nature communications

Article

https://doi.org/10.1038/s41467-025-62968-4

Biosilica nanoparticulate scavengers for the therapy of hepatic ischemia–reperfusion injury in preclinical models

Received: 16 August 2024

Accepted: 6 August 2025

Published online: 16 August 2025

Check for updates

Bingxin Zhou[1,4], Xuchun Chen[2,4], Renyu Ding[3,4], Zhongyun Bi[3,4], Tongyi Zhao[1], Ruilin Zhou[1], Miao Xu[1], Jiawen Li[1], Xinrui Jiang[1] & Heran Li[1]

Hepatic ischemia–reperfusion injury (IRI), involving intracellular Ca^{2+} overload, oxidative stress, inflammatory network, and microcirculation disturbance, remains unsolved clinically. Here, we design a biosilica nanoparticulate scavenger PEI-arg@MON@BA for IRI therapy, via a biomimetic silica–constructing program, based on the cooperative-assembly of cell-free DNA (cfDNA) binding polyethylenimine (PEI), reactive oxygen species (ROS) scavenger tetrasulfur-bridged mesoporous organosilica nanoparticles (MON), intracellular Ca^{2+} chelator BAPTA-AM, and nitric oxide (NO) substrate L-arginine (arg). It targets scavenging cfDNA, ROS, and intracellular Ca^{2+}, and supplying NO, via electrostatic interaction, redox reaction, complexing action, and biotransformation, respectively. Intravenous administered PEI-arg@MON@BA passively targets to the liver, significantly attenuates hepatic damage, decreases oxidative stress, reduces cfDNA-induced TLR9–MyD88–NF-κB signaling, and inhibits the inflammatory cascade in both IRI model and liver transplantation (LT) model in male rats. It also eliminates the danger signals in LT patient serums, and relieves the ischemic injury in human liver tissues, pathing important clinical translation prospects.

Hepatic ischemia-reperfusion injury[1–3]. (IRI) is a common and unavoidable complication after liver transplantation, partial hepatectomy and severe infection[4–6]. Hepatic IRI involves complicated pathogenetic mechanisms, including intracellular Ca^{2+} overload, oxidative stress, inflammatory network, and microcirculation disturbance[4,7–9]. Specifically, (1) intracellular Ca^{2+} overload: During IRI, intracellular Ca^{2+} overload is a complex physiological and pathological event caused by multiple factors, including the impairment of energy metabolism during ischemia (adenosine triphosphate [ATP] depletion, failure of sodium and potassium pump), the increased Ca^{2+} inflow during reperfusion (increased cell membrane permeability, mitochondrial dysfunction), the Ca^{2+} release from endoplasmic reticulum, the activation of calcium-dependent enzymes, and the amplified damage by inflammation and oxidative stress, which all combine to overwhelm the cell's homeostasis and contributed to tissue injury[7,10–13]. (2) Oxidative stress injury: Reactive oxygen species (ROS), which generate through mitochondrial, xanthine oxidase, phagocytic respiration bursts, etc. pathways during both ischemia and reperfusion processes, are considered the most predominant factor for IRI. Excessive ROS can overwhelm and wreck redox homeostasis, induce oxidative damage to DNA, proteins and liquids, and ultimately resulting in deleterious cellular responses, including inflammation, cell death and hepatic failure[7,8,14]. (3) Inflammatory response: The innate immune system recognizes pathogen-associated molecular patterns (PAMPs), damage-associated molecular patterns (DAMPs), and ROS, activating the inflammatory response cascade, leading to the sustained production of inflammatory substances, such as tumor necrosis factor-α (TNF-α), interleukin-1β (IL-1β), interleukin-6 (IL-6), etc[4,7,15–17]. Among DAMPs and

[1]School of Pharmacy, China Medical University, Shenyang, China. [2]Department of Organ Transplantation and Hepatobiliary, The First Hospital of China Medical University, Shenyang, China. [3]Department of Intensive Care Unit, The First Hospital of China Medical University, Shenyang, China. [4]These authors contributed equally: Bingxin Zhou, Xuchun Chen, Renyu Ding, Zhongyun Bi. e-mail: liheranmm@163.com

PAMPs, cell-free DNA (cfDNA) released by damaged cells, which is regarded as a prognostic biomarker of IRI, activates Toll-like receptors-9 (TLR9)-mediated pro-inflammatory signaling in immune cells, and contributes to the magnitude and duration of inflammatiomn[17,18]. Referencing the latest study of a series of inflammatory diseases (e.g., inflammatory bowel disease, sepsis, rheumatoid arthritis, etc.), we reason that targeting cfDNA scavenging represents a promising approach to modulate the imbalanced immune response during IRI[19–21]. (4) Microcirculation disturbance: During liver surgery, microcirculation disturbance caused by the reduced release of vasodilating substances, such as nitric oxide (NO) and prostacyclin, is also an important reason for hepatic failure. NO is a multifunctional signaling molecule, playing an crucial role in regulating microcirculation homeostasis by affecting the mitochondrial function and energy metabolism[4,22]. Growing evidence has discovered that the oral, intravenous or inhalation administration of nitrite, NO, or NO donor drugs attenuates IRI and accelerates the restoration of liver function[23–27]. What's worse, the aforementioned danger signals intimately interwove, create a vicious circle, and trigger pro-inflammatory signaling cascades that drive the pathological progression of IRI[4,9].

A substantial number of studies have made efforts to find strategies against hepatic IRI, including the surgical procedures such as ischemic preconditioning (IPC) and ischemic postconditioning (IPostC), and the application of drugs with functions of anti-oxidation, anti-inflammatory and ameliorating energy metabolism, such as verapamil, glutathione, trimetazidine and ulinastatin[28–31]. Unfortunately, due to the poor operability of pretreatment approaches and the unbeneficial effects of potential therapeutic agents, no effective IRI treatment is approved in clinical practice. Besides, the poor solubility, short half-life, low activities, unsatisfied pharmacokinetics, nonspecific biodistribution, and/or severe side effects of most antioxidants and anti-inflammatory drugs, therapeutic gases, as well as biologics-based immunosuppressive agents after systemic administration also limit their clinical applications[25,32–34]. Nanomedicines, exhibiting a broad spectrum of components and specialties, have gradually emerged as promising alternative measures for hepatic IRI therapy[13,32,35–37]. Recent engineered nanomedicines are mainly focused on alleviating ROS and inflammatory responses with the assistance of advanced nanotechnologies, including novel biological nanostructures, nanoenzymes, and genetic components, which certainly have huge translation prospects once overcoming their obstacles of assembly stability, high cost, quality control, large-scale manufacturing, and potential toxicity and immunogenicity[13,36–40].

We hypothesize that an ideal nanomedicine with simple structure, specific liver distribution and the ability to eliminate multiple pathogenic factors will lead to more attractive IRI therapy. Herein, we design nanoparticulate multiple scavengers (NMSs) via a biomimetic silica–constructing program with abilities of cfDNA-, ROS-, and intracellular Ca^{2+}-scavenging and NO supply through the one-step assembly of DNA-binding polyethylenimine (PEI), ROS scavenger tetrasulfur-bridged mesoporous organosilica nanoparticles (MONs), intracellular Ca^{2+} chelator bis(2-aminophenoxy) ethane-*N*,*N*,*N*,*N*′-tetraacetic acid acetoxymethyl ester (BAPTA-AM, i.e. BA), and NO substrate L-arginine (arg) (Fig. 1). We then characterize the adsorption property, cfDNA-binding, ROS-scavenging, Ca^{2+}-elimination, NO regulation, and antioxidative and anti-inflammatory properties of PEI-arg@MON@BA in vitro and in various cell types. Owing to the passive targeting, PEI-arg@MON@BA highly accumulate in the liver and display superior protective effect against hepatic IRI in the rat model by relieving oxidative stress–induced damage, reducing cfDNA-induced Toll-like receptors-9 (TLR9)–myeloid differential protein-88 (MyD88)–nuclear factor B (NF-κB) signaling, and decreasing the expression of pro-inflammatory cytokines. It also shows protective effect against liver injury in a rat LT model. Particularly, PEI-arg@MON@BA is proven to be stable, biocompatible and biodegradable, and can eliminate the danger signals in patient serums as well as relieve the ischemic injury in the ex vivo human liver tissues, paving an avenue for its potential clinical applications.

Results

Clinical data and patient samples of hepatic IRI

Hepatic IRI is an unavoidable complication in LT and commonly involves liver damage and inflammatory networks[4–7]. We first conducted histopathological studies on hepatic resection of LT patients. According to the pathophysiological process of IRI, we grouped the specimens as tissues without ischemia, tissues with slight ischemia injury (cold ischemic time 2–4 h), tissues with severe ischemia injury (cold ischemic time 6–8 h), and tissues encountered reperfusion, and denoted as Normal, Ischemia 2 h, Ischemia 6 h, Reperfusion groups, respectively (Supplementary Supplementary Table 1). HE staining on ischemic tissues revealed inflammatory cell infiltration and hepatocyte necrosis, worsening with the prolongation of ischemic time (Fig. 2a). After reperfusion, inflammatory cell infiltration, hepatocyte vacuolar degeneration, and hepatocyte necrosis were observed. Furthermore, we highlighted IRI-induced ROS production and hepatocyte apoptosis through DHE and Tunel staining, respectively (Fig. 2b, c, Supplementary Fig. 1). To analyze the immune microenvironments, we performed multiplex IF staining and demonstrated that hepatic IRI led to significant activation of neutrophils and macrophages as well as impaired endothelial integrity (Fig. 2e, Supplementary Figs. 2–4). Particularly, we conducted IHC staining for TLR4/9 as well as the pro-inflammatory markers in hepatic specimens, where expressions of TLR9, MyD88, NF-κB, TNF-a and IL-1β were elevated during IRI, highlighting a pathway of TLR9–MyD88–NF-κB activated by cfDNA. Besides, we collected serum from 20 LT patients and 20 healthy volunteers (Supplementary Table 1). Following the histopathological results, LT patients showed sharply increases in alanine aminotransferase (ALT), aspartate aminotransferase (AST) and total bilirubin (TBIL) levels compared to healthy volunteers, along with evidently elevated pro-inflammatory mediators (including TNF-α, IL-6, interferon-γ [IFN-γ], etc.) and cfDNA levels (Fig. 2f, g, Supplementary Fig. 5). Clinical data confirmed the correlation between serum cfDNA, inflammatory response, and IRI severity in LT patients (Fig. 2h, Supplementary Fig. 6). With the remission of IRI, the patients' liver function recovered gradually, as demonstrated by the simultaneous decreases in biochemical indexes, pro-inflammatory markers, and cfDNA indicators in serum at 7 day post-surgery. Thus, we reasoned that, cfDNA-TLR9 signaling was a potential target for IRI treatment.

Design and biomimetic synthesis of NMSs

Based on the reported pathogenesis and clinical data, we designed a nanomedicine via a biomimetic silica–constructing program, targeting scavenging cfDNA, ROS and intracellular Ca^{2+}, and supplying NO, for IRI treatment (Fig. 3a). We first grafted arg onto PEI through electrostatic interactions and induced crystalline PEI-arg at a low temperature (−20 °C) for a few minutes. As shown in Fig. 3b, h, simple dispersing arg to PEI solution with equimolar NH could afford white solid species PEI-arg, with FTIR characteristic bands of carboxylate at 1558.2 and 1410.4 cm^{-1}. To our knowledge, arg is regarded as a substrate that can be catalyzed by total nitric oxide synthase to produce NO, while PEI is a widely used DNA-binding cationic polyme[41–43]. Meanwhile, we premixed the tetrasulfur-bridged organic silicon source BTES with inorganic TEOS in ethanol. By mixing, the crystalline PEI-arg, consisting of many basic amine groups, itself acted as templates, catalysts and scaffolds to promote the hydrolysis of alkoxysilane and the formation of PEI-arg@MON under neutral pH and ambient conditions, following the biomimetic silicification spirit (Fig. 3c)[44–48]. As an insoluble small-molecule drug, BA could be in situ loaded into PEI-arg@MON by simply dissolving in ethanol during the premixing process, named as PEI-arg@MON@BA. The BA content was measured to be 2.11%.

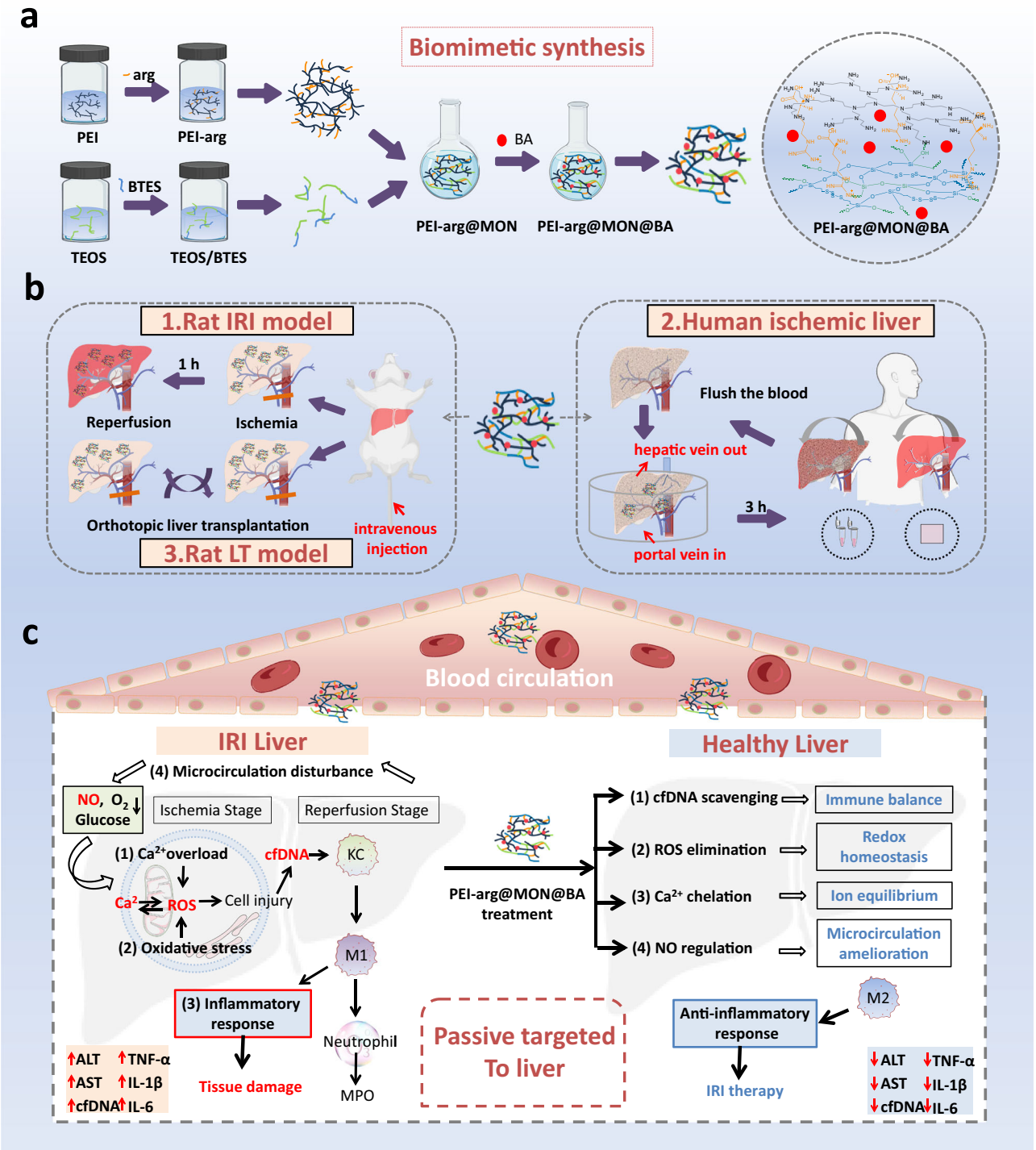

Fig. 1 | Biomimetic synthesis and biological functions of PEI-arg@MON@BA. **a** The schematic diagram and molecular synthetic strategy for PEI-arg@MON@BA. Arg is first grafted onto PEI to get PEI-arg, and BTES is premixed with TEOS. By mixing, the PEI-arg promotes the hydrolysis of alkoxysilane and the formation of PEI-arg@MON. BA is loaded into PEI-arg@MON to get PEI-arg@MON@BA. **b** The treatment protocols on the therapy of PEI-arg@MON@BA on rat IRI model, human ischemic liver and rat LT model. **c** The mechanisms on the generation of liver IRI inflammatory cascade driven by intracellular Ca^{2+} overload, oxidative stress, inflammatory network, and microcirculation disturbance, and the therapeutic effects (passive targeting and scavenging pathogenic factors to suppress inflammation) of PEI-arg@MON@BA against hepatic IRI. Abbreviations: BTES, bis[3-(triethoxysilyl)propyl] tetrasulfide; TEOS, tetraethyl orthosilicate; KC, Kupffer cells; MPO, myeloperoxidase. This Figure created with BioRender.com. https://BioRender.com/a6f1jkd.

Additionally, PEI@Si, generated from depositing TEOS on the catalytic template PEI, and PEI@MON, formed by the dynamic assembly of PEI, BTES and TEOS, were synthesized as references.

TEM and SEM images disclosed the aggregated nanosheet morphologies of PEI@Si, PEI@MON, PEI-arg@MON, and PEI-arg@MON@BA with similar average particle sizes of 20–30 nm (Fig. 3d-f). Vividly, the functional groups were effectively co-condensated with silica deposition, as evidenced by the uniform distribution of elements in the EDS mapping images, with the element content of 18.1%, 38.2%, 38.0%, 4.4%, and 1.3% for Si, O, C, N and S,

https://doi.org/10.1038/s41467-025-62968-4

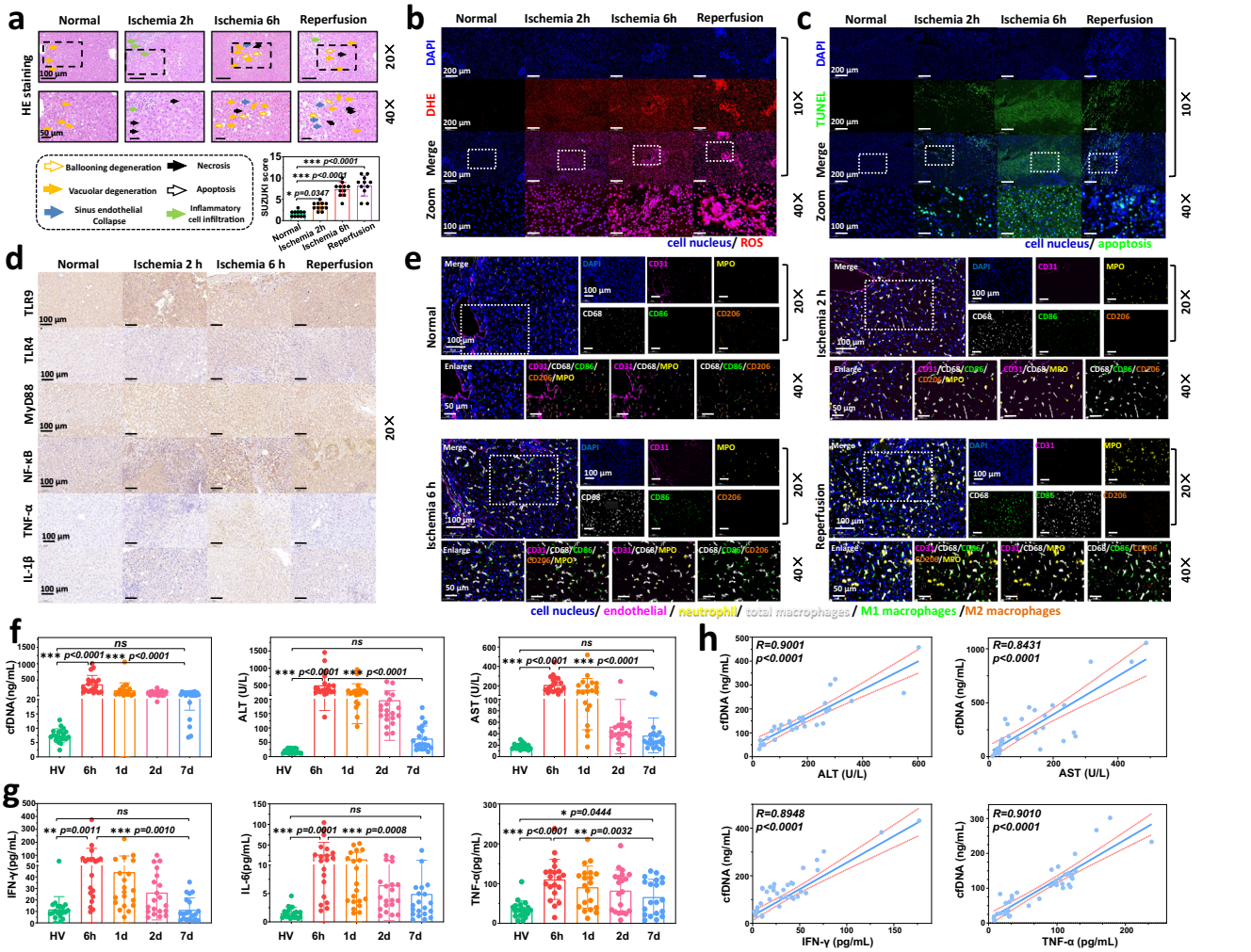

Fig. 2 | LT patient samples associated with IRI. Hematoxylin and eosin (HE, **a**, with the SUZUKI score), dihydroethidium (DHE, **b**) and transferase dUTP nick end labeling (Tunel, **c**) staining images on the liver tissues of LT patients; blue: cell nucleus stained with 4,6-diamidino-2-phenylindole (DAPI), red: ROS, green: apoptotic cells, n = 12 biological replicates. **d** Immunohistochemical (IHC) images on the liver tissues of LT patients, n = 12 biological replicates. **e** DAPI (as a cell nucleus marker, blue), CD31 (as an endothelial marker, pink), myeloperoxidase (MPO, as a neutrophil marker, yellow), CD68 (as a total macrophages marker, white), CD86 (as a M1 macrophages marker, green) and CD206 (as a M2 macrophages marker, orange) multiplex immunofluorescence (IF) images on liver tissues of LT patients, $n = 6$ biological replicates. Serum cfDNA, biochemical indexes (**f**) and serum cytokine levels (**g**) in healthy volunteers (HV, $n = 20$ biological replicates) and LT patients ($n = 20$ biological replicates) at different times after surgery. **h** Linear regression curves illustrating the correlation between serum cfDNA to biochemical indexes and cytokine levels in LT patients. Data presented as the mean ± SD. $^{*}P < 0.05$, $^{**}P < 0.01$ and $^{***}P < 0.001$ by one-way ANOVA. Source data are provided as a Source Data file.

respectively (Fig. 3g, Supplementary Fig. 7). The FTIR spectra of PEI-arg@MON presented typical peaks of ν–Si–O–Si, ν–Si–OH, δ–Si–O–Si, ν-N-H and ν-C-S at 3450, 1076, and 462, 1623.2, and 1075.7 cm^{-1} respectively, which was in good agreement with the XPS finding (Fig. 3i, j). As illustrated in Supplementary Fig. 8, the FTIR spectra of BA showed typical bands at 1768.6 and 3504.6 cm^{-1}, referred to as the –C=O and –NH groups, respectively. Conversely, PEI-arg@MON@BA presented similar spectra to those of PEI-arg@MON with the disappearance of most BA characteristic bands, confirming the incorporation of BA. After multiple modifications, the weight loss (from 20 °C to 700 °C) of PEI@Si, PEI@MON, PEI-arg@MON, and PEI-arg@MON@BA were 43.6% (PEI@Si) to 43.8%, 58.6%, and 64.3%, respectively, indicating the thermo-stability of inorganic silica framework and the successful grafting of organic functional groups (Fig. 3k). PEI-arg@MON@BA experienced intense weight loss on account of the organic modification and BA loading. Meanwhile, their zeta potential decreased stepwise from strongly positive 36.4 mV (PEI@Si) to 17.1, 6.3, and 5.6 mV for PEI@MON, PEI-arg@MON, and PEI-arg@MON@BA, respectively, thus enabling suitability for biomedical applications (Fig. 3l). The mesoporous structure in these NMSs was analyzed by SAXS and nitrogen adsorption/desorption tests (Fig. 3m, n). The results suggested that PEI@Si exhibited distinct mesopores (displaying a typical type IV isotherm with hysteresis loops in the high-pressure section, and a specific surface area [S_{BET}] of ~200 m/g), which was gradually occupied by the grafting groups along with the reduction on S_{BET} and the recession on isothermals (Supplementary Fig. 9). We then investigated the surface/interface properties of NMSs through wettability and oil-water partition coefficient tests. PEI@Si showed high wettability and hydrophilicity related to the large numbers of polar groups (amino group, silanol group, etc.) on the surface, while the hydrophobicity of NMSs was markedly enhanced after the introduction of tetrasulfur groups (Fig. 3o, p, Supplementary Figs. 10, 11). In addition, NMSs were labeled with fluorescent rhodamine isothiocyanate (RITC) through stable covalent bonds, exhibiting good fluorescence stability once performing the in vitro and in vivo tracing tasks (Supplementary Figs. 12, 13). We also stored PEI-arg@MON at

https://doi.org/10.1038/s41467-025-62968-4

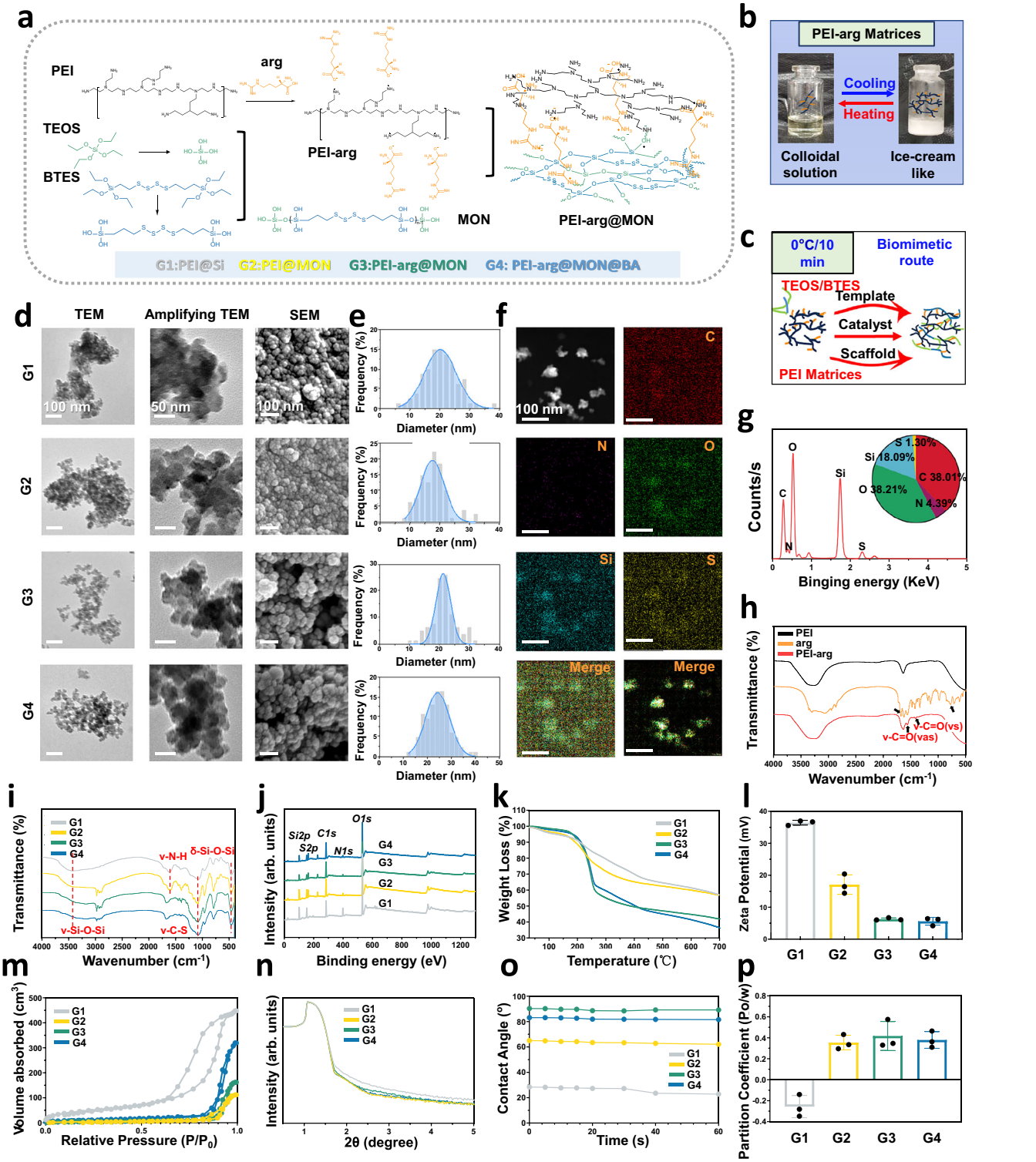

Fig. 3 | The formation and structure of NMSs. a The molecular synthetic route for PEI-arg@MON. Arg is first grafted onto PEI through electrostatic interactions to get PEI-arg, and tetrasulfur-bridged organic silicon source BTES is premixed and polycondensated with the inorganic TEOS in ethanol. By mixing, the crystalline PEI-arg promotes the hydrolysis of alkoxysilane and the formation of PEI-arg@MON. **b** The formation and appearances of crystalline PEI-arg. **c** The versatility of bio-mimetic catalytic template PEI-arg. Transmission electron microscopy (TEM, **d**) and scanning electron microscopy (SEM, **d**) images, and TEM particle size distribution curves (**e**) of NMSs. Energy dispersive spectrometer (EDS) mapping images (**f**) and element distribution (**g**) of PEI-arg@MON@BA. **h**. Fourier-transform infrared spectroscopy (FTIR) spectra of PEI-arg. FTIR spectra (**i**), X-ray photoelectron spectroscopy (XPS) spectra (**j**), thermogravimetric analysis (TGA) curves (**k**), zeta potential (**l**), N_2 adsorption/desorption isotherms (**m**), small angle X-ray scattering (SAXS) patterns (**n**), contact angles-time curves (**o**) and oil-water distributions (**p**) of NMSs. Experiments were repeated three times independently with similar results. Data presented as the mean ± SD. Source data are provided as a Source Data file.

https://doi.org/10.1038/s41467-025-62968-4

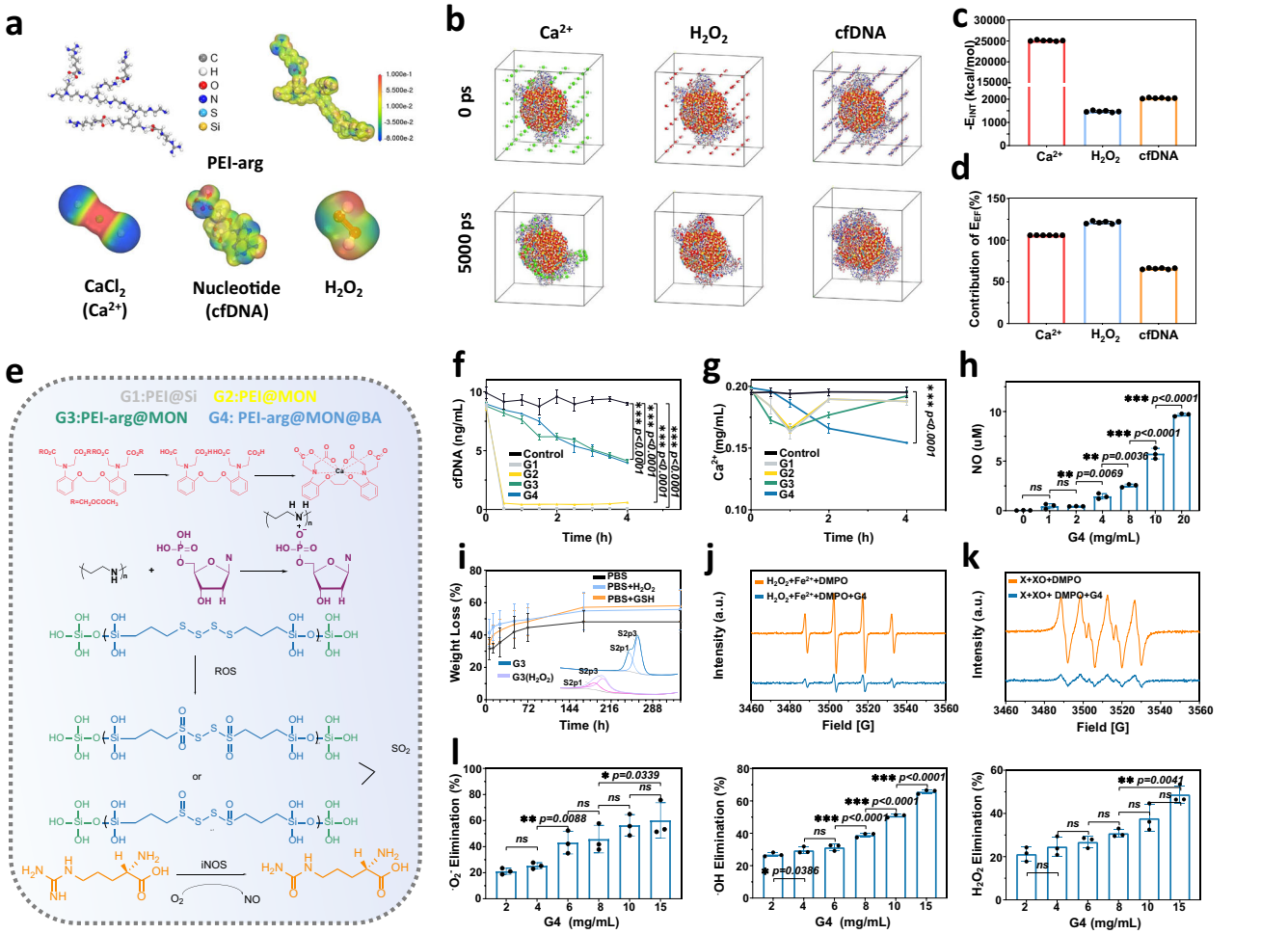

Fig. 4 | In vitro pathogenic factors scavenging performance of NMSs. a. The model building and electrostatic potential analysis on the simulation elements. **b** The molecular dynamics (MD) simulation of pathogenic factors adsorbed to PEI-arg@MON@BA at the initial and equilibrium simulation time. The binding energy (E_{INT}, **c**) and electrostatic force (E_{EF}, **d**) between PEI-arg@MON@BA and pathogenic factors. **e** The equations on the scavenging of various pathogenic factors. BA loaded in PEI-arg@MON@BA chelates intracellular Ca^{2+}. PEI network in NMSs electrostatically interacts with the negatively charged phosphate groups on DNA. Tetrasulfur bonds in NMSs reduce the ROS level via redox reaction, which would be oxidized to sulfoxide or sulfone. Arg in NMSs supplies NO via biotransformation. The scavenging of NMSs on cfDNA (using calf thymus DNA as model DNA, **f**) and Ca^{2+} (**g**). **h** The concentration-dependent NO release of PEI-arg@MON@BA in the presence of hydrogen peroxide. **i** The responsive degradation of PEI-arg@MON in oxidation (H_2O_2) and reduction (GSH) environments and the valence state of sulfur element before and after incubation with H_2O_2. **j** Electron paramagnetic resonance (EPR) spectra of the mixed solution of Fe^{2+}, H_2O_2, and 5,5-dimethyl-1-pyrroline-N-oxide (DMPO) in the presence or absence of PEI-arg@MON@BA. **k**. EPR spectra of the mixed solution of xanthine (X), xanthine oxidase (XO), and DMPO in the presence or absence of PEI-arg@MON@BA. **l** The concentration-dependent ROS radicals ($\cdot O_2^-$, ·OH and H_2O_2) scavenging capacities of PEI-arg@MON@BA. Experiments were repeated three times independently with similar results. Data presented as the mean ± SD. $^*P < 0.05$, $^{**}P < 0.01$ and $^{***}P < 0.001$ by one-way ANOVA. Source data are provided as a Source Data file.

room temperature for 6 months, and TEM images and FTIR spectra discovered clear nanosheet mesoporous silica structure without obvious degradation (Supplementary Fig. 14). Collectively, through the dynamic assembly of PEI, arg, BTES, TEOS and BA, the functional components were co-condensated with silica deposition via a biomimetic program, boasting huge potential for simultaneous scavenging multiple pathogenic factors.

NMSs scavenge pathogenic factors in vitro

With the aim of comprehensively understanding the surface/interface properties of NMSs, we first proposed MD simulation to explore the physical interactions between PEI-arg@MON@BA and various pathogenic factors. A cluster structure of tetrasulfur-bridged SiO_2 was built to imitate the main body of the PEI-arg@MON@BA nanosheet, which was then grafted with the functional modules of PEI-arg and BA (Supplementary Fig. 15). The structures of cfDNA, H_2O_2, and Ca^{2+} were simplified to nucleotide, H_2O_2, and $CaCl_2$ molecules, respectively (Fig. 4a). The adsorption configuration was monitored during 5000 ps of equilibrium, where all three substances were adsorbed tightly around the PEI-arg@MON@BA cluster (Fig. 4b, Supplementary Fig. 16). Consistently, the E_{INT} between the clusters and nucleotide, H_2O_2, and $CaCl_2$ were −25022.24, −2056.07, and −1488.82 kcal/mol, respectively, accounting for the definite adsorption effect (Fig. 4c). The computation results suggested a ~ 66% contribution of the E_{EF} and a ~ 34% contribution of van der Waals' force (E_{VDW}) between the cluster and nucleotide (Fig. 4d, Supplementary Fig. 17, Supplementary Table 5). However, in the case of H_2O_2 and $CaCl_2$, electrostatic forces were absolute dominant. Besides, plenty of hydrogen bonds were formed between the cluster and cfDNA, as well as the cluster and H_2O_2, which were favorable for the stability of the system (Supplementary Table 6). Taken together, these results theoretically demonstrated the affinity and adsorption tendency between PEI-arg@MON@BA and the pathogenic factors, providing prerequisites for the scavenging of these substances (Fig. 4e).

As mesoporous materials, the adsorption capacity of the NMSs was briefly studied, where noticeable color decline was directly observed after incubating with the amphoteric charged dye rhodamine B (RhB) and the positively charged dye evans blue (EB, Supplementary Fig. 18). Subsequently, we evaluated the functions of NMSs in eliminating cfDNA and Ca^{2+}. To our knowledge, abundant positively charged amino groups on PEI could electrostatically interact with the negatively charged phosphate groups on DNA[42]. According to Fig. 4f, NMSs all showed binding affinities for the model cfDNA. PEI-arg@MON as well as PEI-arg@MON@BA, exhibiting weak positive charges, had lower DNA-binding affinities than PEI@Si, but would cause less cytotoxicity and safety hazards than the strongly positive NMS[49]. We tested the Ca^{2+} scavenging ability of PEI-arg@MON@BA via complexometric titration using $CaCl_2$ as a substrate, ethylenediamine tetraacetic acid (EDTA, i.e., Y^{4-}) as a titrating solution, and calconum (NN) as an indicator. PEI-arg@MON@BA effectively reduced the content of free Ca^{2+} in the system in vitro, thus proving to be a powerful Ca^{2+} chelator (Fig. 4g). We introduced a Griess kit to assess the ability of PEI-arg@MON@BA to release NO in the presence of H_2O_2. As can be seen in Fig. 4h, the amount of released NO increased with the increasing concentration of PEI-arg@MON@BA, indicating its function as NO donor[50].

To study the antioxidant ability of NMSs, 2,2′,azino-bis(3-ethylbenzothiazoline-6-sulfonic acid (ABTS), 2,2-diphenyl-1-picrylhydrazyl (DPPH) and 3,3′,5,5′-tetramethylbenzidine (TMB) analysis were performed. From a direct observation on the color fading of $ABTS^{\bullet+}$, DPPH and TMB agents from blue to colorless, from dark violet to yellow, and from colorless to blue, respectively, we identified the favorable antioxidant capacity ability of PEI-arg@MON@BA (Supplementary Fig. 19, 20). Further calculation from the absorbance decreases indicated that the radical scavenging efficiency was positively correlated with the concentration of NMSs, highlighting its valid antioxidant ability. Similarly, the color and absorbance of the DPPH agent after incubation with PEI-arg@MON@BA changed over time because of the radical scavenging activity (Supplementary Fig. 21). NMSs reduced the ROS level in the system because the tetrasulfur bonds would be oxidized to highly hydrophilic sulfoxide or sulfone, as evidenced by the appearing characteristic peak of sulfoxide (v−S=O, 1040.4 cm^{-1}) and sulphone (v−S=O, 1347. 6 cm^{-1}) as well as the disappearance of tetrasulfur bond, in the FTIR spectra after incubating PEI-arg@MON with the H_2O_2-containing mediums (Supplementary Fig. 22). Meanwhile, the valence of sulfur element changed from +2 to +4 ~ 6 valence (Fig. 4i)[51–53]. Additionally, NMSs became more hydrophilic in the oxidation environment (Fig. 4i, Supplementary Fig. 22). Compared to the degradation of NMSs in pH 7.4 phosphate-buffered saline (PBS), PEI-arg@MON underwent rapid degradation from 31.85% to 45.02% and 40.16% within 6 h in mimicking oxidation (H_2O_2) and mimicking redox (glutathione [GSH]) conditions, respectively, on account of the oxidation and reduction sensitivity of tetrasulfur bonds, enabling their potential for ROS binding and removal (Fig. 4i, Supplementary Fig. 23). To study the single radical scavenging of PEI-arg@MON@BA, we further electron paramagnetic resonance (EPR) tests, which demonstrated the effective ·OH, and $\cdot O_2^-$ scavenging capacity of PEI-arg@MON@BA with significantly reduced EPR signal intensity (Fig. 4j, k). For quantitative analysis, we applied PEI-arg@MON@BA to eliminate single free radicals (including H_2O_2, ·OH, and $\cdot O_2^-$) and determined the free radical contents by testing with assay kits. The results discovered that, PEI-arg@MON@BA reduced the levels of various radicals in a concentration-dependent manner (Fig. 4l).

Encouraged by the cfDNA-, ROS-, and Ca^{2+}-scavenging of NMSs in vitro, we collected the LT patient serum and incubated the serum solution with NMSs (Supplementary Fig. 24). When NMSs were present, we unsurprisingly found that the cfDNA and radical levels gradually decreased, suggesting the effective clearance. To sum up, by employing NMSs as nanomedicines, the pathogenic factors cfDNA, ROS, and Ca^{2+} were highly eliminated via electrostatic interaction, redox reaction, and complexing action, respectively.

NMSs regulate redox balance and inflammation in cells

As macrophage is a central cell type in directing host inflammatory and immune processes, we performed the cellular evaluations on mouse RAW 264.7, human monocytic leukemia cells (THP-1) and Kupffer cells of mouse liver (KC) to gain insights into the NMSs-mediated host response (Supplementary Fig. 25)[54]. We initially qualitatively, quantitatively and locally examined the internalization efficiency of NMSs after incubation with RAW 264.7 cells for 4 h using CLSM, FCM, and bio-TEM, respectively. As shown in Fig. 5a, b, PEI@Si and PEI@MON displayed poor RITC fluorescent signals, while PEI-arg@MON as well as PEI-arg@MON@BA emitted bright red fluorescent signals distributed near the nucleus or intra nucleus after 4 h of culture, implying that they effectively crossed the cell membrane and accumulated in the cells. Similar results were proved by FCM, where the uptake amounts of PEI@Si, PEI@MON, PEI-arg@MON, and PEI-arg@MON@BA were 19.41%, 58.9%, 625%, and 89.8%, respectively (Fig. 5c). From the bio-TEM images of NMSs, we directly observed the efficient cellular internalization of PEI-arg@MON and PEI-arg@MON@BA, where nanosheets aggregated in cells without destroying the membrane structures (Fig. 5d, Supplementary Fig. 26). NMSs with arg modification exhibited superior cellular uptake than PEI@Si and PEI-MON, probably due to the cell-penetrating peptide effect of the poly-arginine structure (where the positive surface charge of NMSs electrostatically interacted with the negatively charged cell membrane, meanwhile, the guanidine groups formed hydrogen bonds with the phosphate groups on the cell membrane)[55]. Furthermore, bright red fluorescent signals from RITC labeled PEI-arg@MON and PEI-arg@MON@BA were also noticed around the nucleus of THP-1 and KC cells, indicating good cellular internalization capacity (Supplementary Fig. 27). The uptake amounts of PEI-arg@MON and PEI-arg@MON@BA were measured to be 19.7% and 23.9% in THP-1 cells and 22.8% and 19.4% in KC cells (Supplementary Fig. 27). To investigate whether the forceful cellular uptake of NMSs would threaten cell viability, we carried out the cell counting kit-8 (CCK-8) study, ROS measurement, and fluorescence live/dead assay on RAW 264.7 cells, which all demonstrated that NMSs showed negligible influence on cell viability (Supplementary Figs. 28, 29). What's more, NMSs demonstrated high cytocompatibility (cell viability higher than 90.45%) at 0-80 μg/mL after exposed to THP-1, KC and AML12 (mouse hepatocyte) cells (Supplementary Fig. 30).

Based on the good cytocompatibility and high cellular internalization of NMSs, we investigated its antioxidant effect, where LPS was applied to induce inflammatory responses and cell death (Supplementary Fig. 31). According to Fig. 5f and Supplementary Figs. 29, 32, 33, in RAW 264.7, THP-1 and KC cells, potent green fluorescence generated from DCFH-DA was found after the addition of LPS, indicating the existence of intracellular ROS. The fluorescence live/dead assay presented high levels of cell death (Fig. 5h, Supplementary Figs. 27, 30, 31). Consistent with the in vitro ROS−scavenging results, treatment of PEI-arg@MON and PEI-arg@MON@BA remarkably eliminated ROS, as manifested by the negligible green fluorescence. After PEI-arg@MON@BA treatment, we also noticed decreased Ca^{2+} signal and increased NO signal with the assistance of Fluo-4 and DAF-FMDA probes, respectively, accounting for its Ca^{2+} chelating and NO production capacities (Fig. 5e, g, Supplementary Figs. 29, 32, 33). The live/dead cell staining images revealed that almost no dead cells were observed before and after LPS exposure when PEI-arg@MON@BA was present, illustrating both the negative cytotoxicity and evident cellular protection ability (Fig. 5h, Supplementary Figs. 29, 32, 33). We then quantified the cell protective ability of NMSs against LPS using the CCK8 assay, where the survival rates were improved from 51.3%, 57.3%, 64.2% and 67.5% to 72.1%, 72.3%, 83.6% and 79.4% for RAW 264.7, THP-1, KC and AML12 cells after administration of PEI-arg@MON@BA during

https://doi.org/10.1038/s41467-025-62968-4

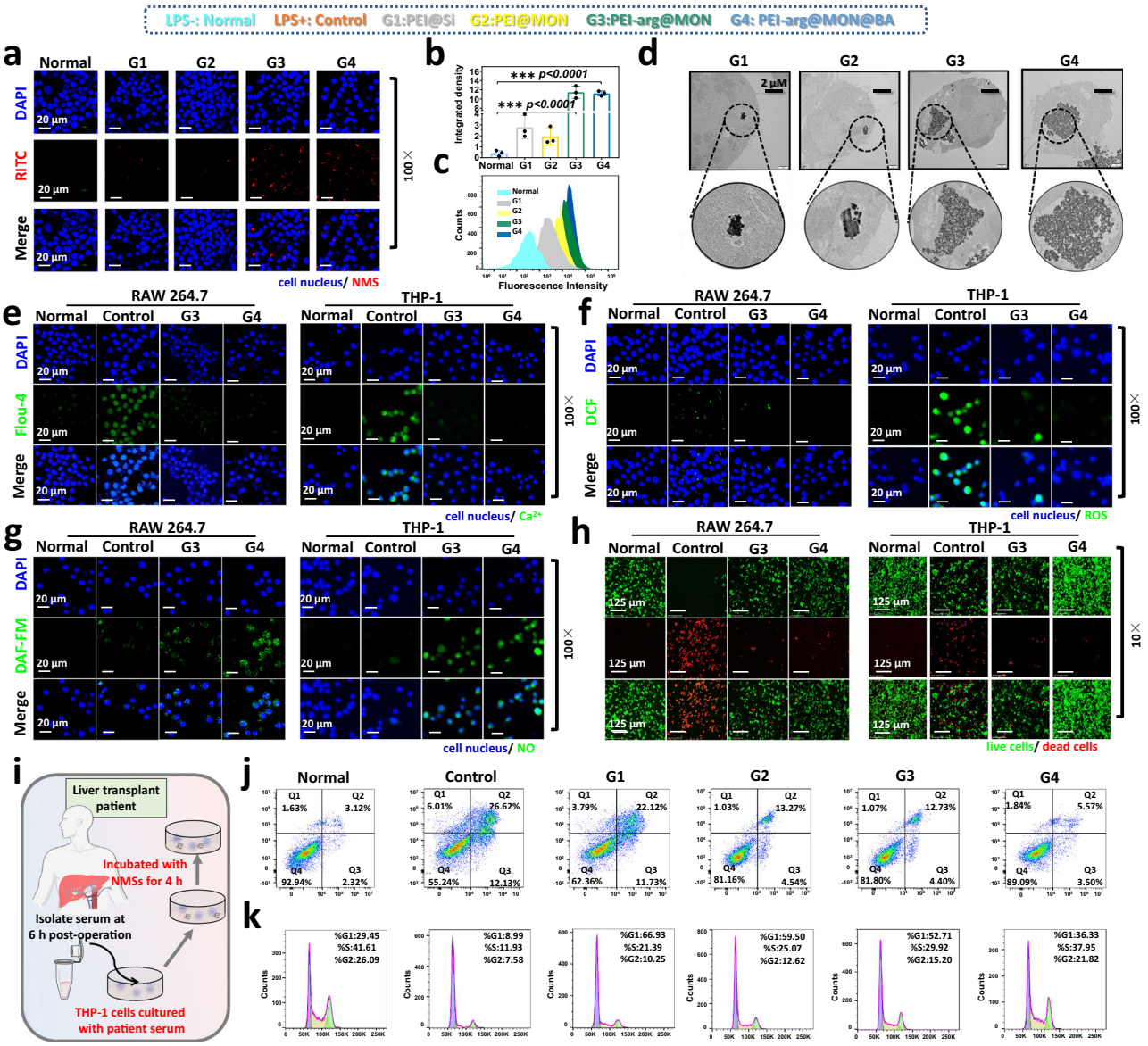

Fig. 5 | Intracellular pathogenic factors-scavenging performance of NMSs. Confocal fluorescence microscopy (CLSM) images (**a**) and the semiquantitative fluorescence analysis (**b**) of the cellular uptake of NMSs on RAW 264.7 cells; blue: cell nucleus stained with DAPI, red: RITC labeled NMSs, scale bar 20 μm. **c** Flow cytometry (FCM) analysis on the RAW 264.7 cellular internalization of NMSs. **d** Bio-TEM images on the cellular uptake of NMSs on RAW 264.7 cells. DAF-FMDA staining images of NMSs treated on RAW 264.7 and THP-1 cells to indicate the NO production with in present of LPS (**e**); blue: cell nucleus, green: intracellular NO, scale bar 20 μm; 7′hdichlorofluorescein diacetate (DCFH-DA, i.e., DCF) staining images of NMSs treated RAW 264.7 and THP-1 cells to indicate intracellular ROS in present of LPS (**f**); blue: cell nucleus, green: intracellular ROS, scale bar 20 μm; Fluo-3 staining images of NMSs treated RAW 264.7 and THP-1 cells to indicate intracellular Ca^{2+} influx in present of LPS (**g**); blue: cell nucleus, green: intracellular Ca^{2+}, scale bar 20 μm; Calcein-AM/PI staining images of NMSs treated RAW 264.7 and THP-1cells to indicate the live/dead cells in present of LPS (**h**); green: live cells, red: dead cells, scale bar 125 μm. **i** Treatment protocols on the irritation of LT patient serum on THP-1 cells. Apoptosis (**j**) and cell cycle (**k**) of THP-1 cells after irritation of LT patient serum. Experiment was repeated three times independently with similar results. Data presented as the mean ± SD. $^{*}P < 0.05$, $^{**}P < 0.01$ and $^{***}P < 0.001$ by one-way ANOVA. Source data are provided as a Source Data file. **i** Created with BioRender.com. https://BioRender.com/5qzx7z0.

the LPS processes, respectively (Supplementary Figs. 34, 35). In addition, NMSs also alleviated oxidative stress, restored superoxide dismutase (SOD)/ catalase CAT (activity), and downregulated TNF-α level owing to its remarkable antioxidant tendency and cellular internalization ability (Supplementary Fig. 36). In particular, we also conducted cell interaction experiments by co-culturing AML12 and RAW 264.7 cells. In co-culture systems of AML12 and RAW264.7 cells, TNF-α and IL-6 mRNA levels in AML12 hepatocytes exhibited significant elevation compared to LPS stimulation alone, with supernatant ALT measurements demonstrating a parallel trend. The administration of PEI-arg@MON@BA effectively mitigated both hepatic injury and inflammatory markers. These results corroborated the critical role of macrophages as mediators in hepatocellular inflammatory damage and substantiate the therapeutic efficacy of NMSs within this pathological pathway (Fig. 47).

Given the promising results of NMSs in regulating redox balance and relieving inflammation in cells, we cultured THP-1 macrophages with the patient serum and evaluated the cell apoptosis and cell cycle via FCM (Fig. 5i). According to Fig. 5j, cell apoptosis was significantly relieved by treating with PEI-arg@MON@BA, showing good agreement with the cell viability data after LPS treatment. Particularly, various pathogenic factors in patient serum caused excessive cell

https://doi.org/10.1038/s41467-025-62968-4

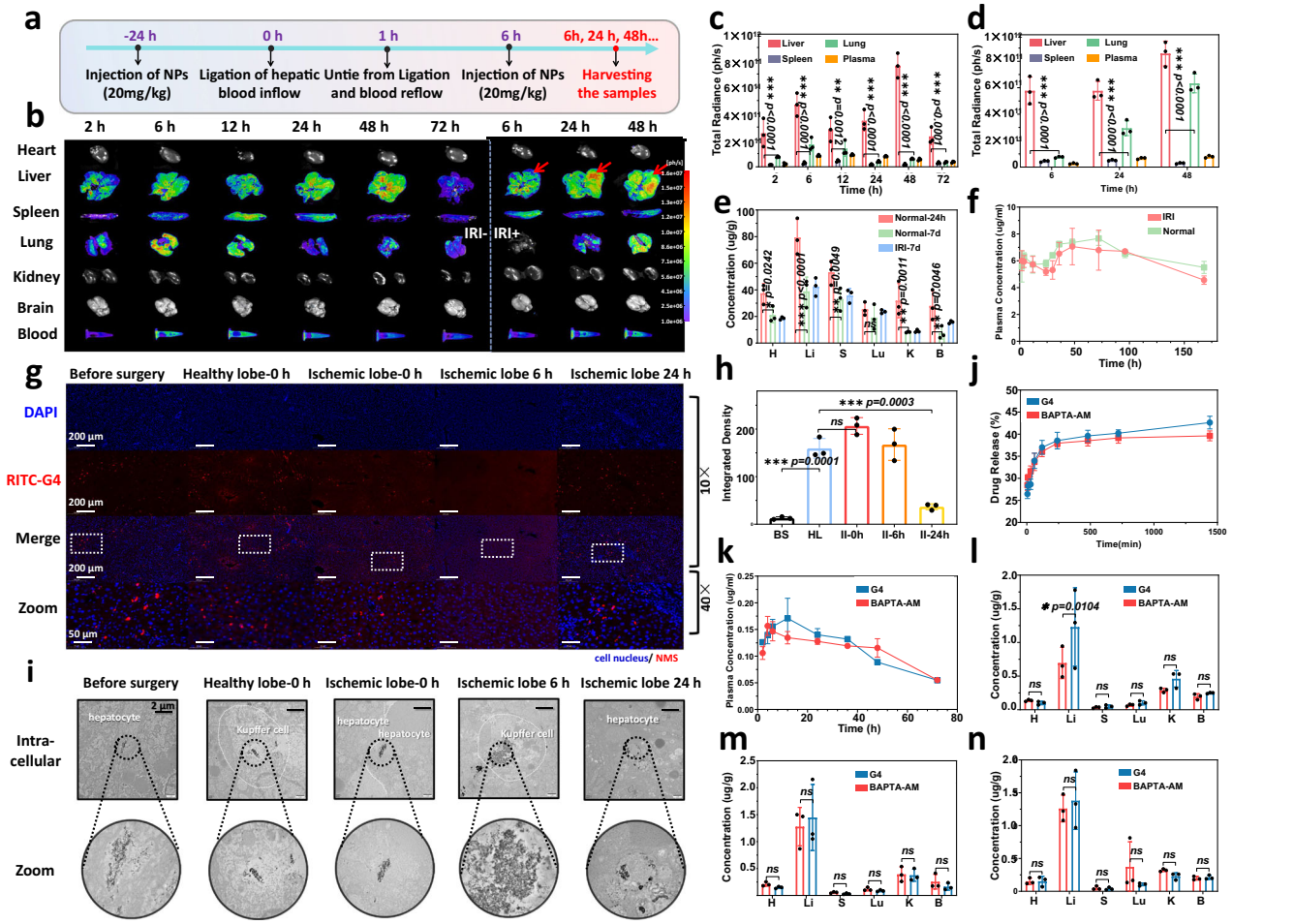

Fig. 6 | Passive targeting and biological fate of NMSs. a Treatment protocols on the rat IRI model. Fluorescence images (**b**) and the semiquantitative fluorescence analysis (**c** healthy rats, **d** IRI rats) of RITC labeled PEI-arg@MON@BA in the main organs and blood of rats. Quantitative analysis on the distribution of PEI-arg@MON@BA in the main organs (**e**) and blood (**f**) of healthy rats and IRI rats detected by inductively coupled plasma mass spectrometry (ICP-MS). CLSM images (**g**) and the semiquantitative fluorescence analysis (**h**), BS, HL,II represent before surgery, healthy lobe and ischemic lobe, respectively) of RITC labeled PEI-arg@MON@BA in the liver lobes of rats during IRI; blue: cell nucleus, red: RITC labeled PEI-arg@MON@BA. **i**. The bio-TEM images of PEI-arg@MON@BA in the liver lobes of rats during IRI. **j** In vitro release of BA from PEI-arg@MON@BA in pH 7.4 PBS. $n = 3$ biologically independent animals. Data presented as the mean ± SD. $^{*}P < 0.05$, $^{**}P < 0.01$ and $^{***}P < 0.001$ by one-way ANOVA. Plasma concentration-time profiles (**k**) and distribution (**l**, **m**, **n** at 2, 6, and 24 h post intravenous injection, respectively; H, Li, S, Lu, K and B represent heart, liver, spleen lung, kidney and brain, respectively) of BA from PEI-arg@MON@BA. $n = 3$ biologically independent animals. Data presented as the mean ± SD. $^{*}P < 0.05$, $^{**}P < 0.01$ and $^{***}P < 0.001$ by two-tailed Student's t-test. Source data are provided as a Source Data file.

apoptosis with the apparent change in cell cycle to G2M suppression, while treatment with NMSs significantly reduced the apoptosis rate and helped to restore normal cell cycle (Fig. 5k, Supplementary Fig. 38). Overall, NMSs was believed to possess superior cytocompatibility and cellular internalization, and was found to relieve oxidative stress and ameliorate inflammatory response.

NMSs passively target and accumulate in the liver

We detected the distribution and accumulation of NMSs in the rats' livers. To study the bio-distribution of NMSs in the healthy liver, PEI-arg@MON@BA was administrated to rats via intravenous injection at a dose of 20 mg/kg. We also established the rat hepatic IRI model according to the protocol by blocking 70% of structures in the portal triad (hepatic artery, bile duct, and portal vein) to the left and median liver lobes for 60 min using a microvascular clamp, followed by reperfusion after removing the clamp (Fig. 6a). The liver color in the central lobe and the left lobe immediately changed from red to reddish-brown (ischemic phase) and red reperfusion phase during modeling (Supplementary Fig. 39). For therapy, IRI rats received twice intravenous injections of NMSs (20 mg/kg) at 24 h before and 6 h after the IRI surgery, respectively.

NMSs distributions in the major organs were qualitatively and quantitatively analyzed using the IVIS Lumina Series III Living Image System and ICP-MS, respectively. Overall, NMSs were highly distributed in the organs within the reticuloendothelial system (RES). To be specific, in healthy rats, PEI-arg@MON@BA rapidly distributed in the liver, gradually increased in a time-dependent manner due to the passive targeting of NMSs, and metabolized from the liver at 72 h post administration (Fig. 6b, c). Meanwhile, a certain amount of NMSs was distributed in spleen and lung, where the macrophage was rich. We found potent fluorescence signals (total fluorescence intensity 5.77E + 11 ph/s/) of NMSs in the liver at 24 h post dose and therefore subjected to the hepatic modeling surgery to obtain IRI rats. The amount of NMSs in the main organs of IRI rats was reduced at 6 h after surgery and enhanced distinctly at 24 h because of the second dose (Fig. 6b,d). ICP-MS also confirmed the accumulation of PEI-arg@MON@BA in the liver and spleen at 24 h, which was metabolized via liver and poorly distributed in the blood

and all organs at 7 days post administration (Fig. 6e,f, Supplementary Table 7).

We then sliced the liver lobe into ultrathin sections and focused our study on the accumulation of PEI-arg@MON@BA in the liver via CLSM and bio-TEM. As shown in Fig. 6g, h, the fluorescence intensity of PEI-arg@MON@BA was significantly strong at all time points and effectively accumulated in both the normal liver lobe and the IRI lobe. We unsurprisingly observed a substantial number of aggregated nanosheets, most likely PEI-arg@MON@BA, entered and distributed in liver tissues from the bio-TEM images, which were mainly internalized by hepatocytes and Kupffer cells (Fig. 6i). Meanwhile, the bio-TEM images indicated no damage to cell structure or membrane integrity after exposure to NMSs. In one word, the liver, owing to its large weight, metabolic function, and rich RES, was the main passive targeted organ for NMSs.

Subsequently, we investigated the release and bioavailability of BA in vitro and in vivo. The drug release of PEI-arg@MON@BA was analyzed in pH 7.4 PBS by employing pure BA as a reference, which was slightly increased after loading into PEI-arg@MON (Fig. 6j). 42.6% of the drug released from PEI-arg@MON at 24 h. We assessed the bioavailability of PEI-arg@MON@BA by systematically analyzing the pharmacokinetics, distribution, and metabolism of the drug. After intravenous injection, BA rapidly entered the bloodstream and peaked at 4 h, whereas PEI-arg@MON@BA, with slow-release ability, prolonged the peak concentration time (T_{max}) to 8 h and increased the maximum blood concentrations (C_{max}) from 0.158 to 0.176 μg/ml (Fig. 6k, Supplementary Table 8). Furthermore, in the PEI-arg@MON@BA group, BA showed substantially increased accumulation in all main organs at 2 h, especially in the liver, where the drug amount was 43.5% higher than that of BA (Fig. 6l). At 6 and 24 h, rats in the BA group displayed higher drug content in the heart, spleen, kidney and brain (Fig. 6m, n). Conversely, BA in the PEI-arg@MON@BA groups passively targeted and accumulated in the liver, consistently showing higher drug content compared to the BA group.

NMSs show good biocompatibility in vivo

In light of the intravenous injection delivery route, we first analyzed the hemocompatibility of NMSs. Initially, we used TEM and FTIR to investigate the peripheral blood stability of NMSs after 48 h co-incubation with rat plasma and human plasma, which discovered no significant change on their appearance and structure (Supplementary Fig. 40). Besides, the hemolysis rates of NMSs were slightly concentration-dependent but following the standard for biomaterials: ISO 10993–4:2002.40 (Supplementary Fig. 41). Even at high dose (800 μg/mL) for biomedical applications, the hemolysis rates were <6%, showing good biocompatibility. To exclude a risk of thrombus, we carried out coagulation tests and thrombus tests, respectively. In a typical run, we collected the rat blood after intravenous injection of PEI-arg@MON@BA for 4 h and examined the coagulation indicators (prothrombin time [PT], activated partial thromboplastin time [APTT], thrombin time [TT], fibrinogen [FIB]). As shown in Supplementary Fig. 40, there was no significant difference on the four blood coagulation indexes between PEI-arg@MON@BA injected rats and control rats. Thrombin-antithrombin complex (TAT), D-dimer (D2D), and thrombomodulin (TM) Elisa kits related to thrombus also discovered no inopectic diathesis of PEI-arg@MON@BA injected rats compared to normal rats (Fig. 52).

To investigate the potential in vivo toxicity and side effects of NMSs, rats were intravenously injected with PEI-arg@MON@BA at a double dose of 40 mg/kg and executed on the 14th day. No sudden deaths, unusual behaviors, or significant weight loss were observed during the experimental period. We then collected their blood and major organs for hematological and biochemical tests, and histopathological examinations. The hematological parameters as well as biochemical indicators were all within the reference ranges and showed no significant difference compared to the control group (Supplementary Fig. 43). The main organs appeared to be normal in appearance and discovered no significant histopathological abnormalities or damage in the HE staining (Supplementary Fig. 43).

Finally, we carried out systematically lung function testes of PEI-arg@MON@BA via HE and IHC (TNF-α, IL-1β, masson, and α-SMA, referring to both inflammation and fibrosis) at 24 h and 14 days post administration. Rats in the PEI-arg@MON@BA group showed normal lung structure without marked edema, inflammation, or fibrosis, and the inflammation and fibrosis markers were negative without obvious difference compared to the control group (Supplementary Figs. 44–46). We also collected the pulmonary perfusion fluids and measured the inflammatory cytokines, including TNF-α, IL-6, IL-1β, IL-6, IL-17A IL-10, which indicated that rats exposed to PEI-arg@MON@BA showed no significant inflammation compared to the control group (Supplementary Fig. 47). Collectively, in all these experiments in vitro and in vivo, NMSs lacked any indication of toxicity.

Protective effect of NMSs on rat hepatic IRI model at 6 h post IRI

Encouraged by the promising antioxidant capacity of NMSs in vitro, we processed to study their protective effects against rat hepatic IRI in vivo by employing warm ischemia-reperfusion surgery. We first collected the liver sample in the control group before and immediately after removing the clamp. HE staining suggested local hepatocyte necrosis and hepatocyte vacuolar degeneration, indicating substantial damages raised by both ischemia and reperfusion (Supplementary Fig. 48). With the aim of evaluating the therapeutic effect of NMSs, we separated the blood and tissue samples from rats to analyze the pathological microenvironment, inflammatory response and liver functions at 6 (NMSs given once) and 24 h (NMSs given twice) after surgery, respectively.

At 6 h after reperfusion, severe liver damage was found in rats in the control group, where massive necrosis of hepatocytes, dissociation of hepatic cords, endothelial collapse and disappearance of hepatic sinuses were observed in the HE staining (SUZUKI score 7.8, Fig. 7a, b, Supplementary Fig. 49). Synergistically, the common clinical indices for liver health, such as ALT and AST, remarkably increased from 60.3 to 1121.5 U/L (ALT) and from 78.2 to 1236.4 U/L (AST) compared to the untreated normal group, implying severe liver damage (Fig. 7c, Supplementary Fig. 50). PEI@MON partly attenuated the damage, likely attributing to its ROS-scavenging effect. In comparison, PEI-arg@MON and PEI-arg@MON@BA alleviated tissue injury, as evidenced by the almost normal liver tissues with slight vacuolar degeneration occurring in some hepatocytes (SUZUKI score, 0.33) and the significantly reduced ALT and AST levels (Fig. 7b–e, Supplementary Figs. 49–51). We also noticed obviously reduced cfDNA levels in rat serum with the acceptance of NMSs therapy (Fig. 7d). In order to study dose-dependent treatment, we conducted the 1/2 dose and 1/5 dose of PEI-arg@MON@BA for IRI treatment, which strongly illustrated its dose-dependent therapy (Supplementary Figs. 52, 53). The disease indexes of rats in Control, 1/5 dose, 1/2 dose and 1 dose PEI-arg@MON@BA groups were 10.7, 9.3, 7.0 and 0.3, respectively (Supplementary Fig. 52). By the way, we proposed that, BAPTA (without AM modification) can effectively enter the cytoplasm through the endocytosis of NMSs, and expansively prepared a nanomedicine PEI-arg@MON@BAPTA by encapsulating BAPTA with lower synthesis cost instead of BAPTA-AM into PEI-arg@MON, which showed similar therapeutic effects with those of PEI-arg@MON@BA groups (Supplementary Figs. 54, 55).

To our knowledge, the excessive generation of ROS is recognized as a vital mechanism to cause tissue damage during IRI[7]. We studied the antioxidative activity of NMSs in vivo using DHE staining. Consistent with the clinical pathophysiological processes in LT patients, the liver tissues of IRI rats in the control group showed pronounced

https://doi.org/10.1038/s41467-025-62968-4

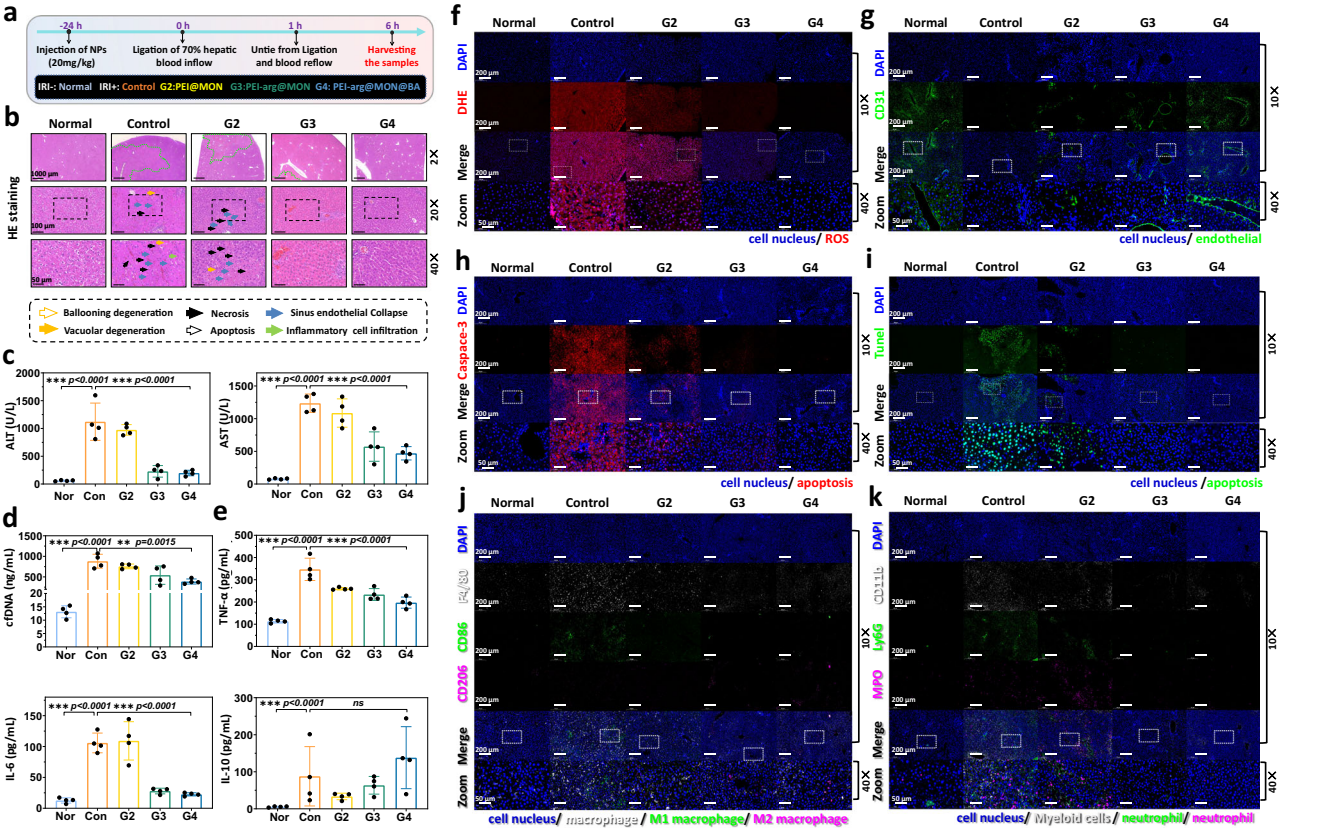

Fig. 7 | Treatment efficacy of NMSs against IRI rats at 6 h post-surgery. a. Treatment protocols on the rat IRI model harvested at 6 h post-surgery. HE staining images (**b**), ischemic areas, SUZUKI score, and serum biochemical indexes (**c**), cfDNA level (**d**), and cytokine levels (**e**) of IRI rats after 60 min of ischemia and 6 h of reperfusion. $n = 3$ (HE staining) or 4 biologically independent animals. **f** DHE staining images of the liver tissues of IRI rats; blue: cell nucleus, red: ROS. **g** CD31 staining images of the liver tissues of IRI rats; blue: cell nucleus, green: endothelial. **h** Caspase-3 staining images of the liver tissues of IRI rats; blue: cell nucleus, red: cell apoptosis. **i** Tunel staining images of the liver tissues of IRI rats; blue: cell nucleus, green: apoptotic cells. **j** F4/80 (as a M1 macrophages marker, white), CD86 (as a M1 macrophages marker, green) and CD206 (as a M2 macrophages marker, purple) staining images of the liver tissues of IRI rats to indicate macrophages. **k** CD11b (as a myeloid cells marker, white), Ly6G (as a neutrophil marker, green) and MPO (as a neutrophil marker, purple) staining images on liver tissues of IRI rats to indicate neutrophil. $n = 3$ biologically independent animals. Data are presented as the mean ± SD. $^{*}P < 0.05$, $^{**}P < 0.01$ and $^{***}P < 0.001$ by one-way ANOVA. Source data are provided as a Source Data file.

fluorescent signals of ROS, while the superoxide signals sharply decreased in the PEI-arg@MON and PEI-arg@MON@BA groups (Fig. 7f, Supplementary Fig. 56). Tunel and Caspase-3 staining showed that the massive apoptosis of hepatocytes induced by IRI was intervened with the help of NMSs (Fig. 7h, i, Supplementary Figs. 56, 57). We then conducted IF studies corresponding to the cellular phenotypes on tissue samples. As shown in Fig. 7g, j, k and Supplementary Fig. 57, distinct activation of macrophages was observed in IRI rats in the control group, where the majority of macrophages were identified as pro-inflammatory M1 type. Meanwhile, neutrophil infiltration was infiltrated in the damaged areas. Obvious growth expression of pro-inflammatory cytokines, including TNF-α, IL-6, IFN-γ and monocyte chemoattractant protein-1 (MCP-1), etc., were highlighted using enzyme-linked immunosorbent assay (ELISA), thus leading to more liver damage in the continued circle (Fig. 7e, Supplementary Fig. 51). Conversely, PEI-arg-MON@BA inhibited the activation of macrophages, the recruitment of neutrophils, and the subsequent apoptotic processes, and was contributed to the downregulation of the inflammatory response (Fig. 7e, j, k, Supplementary Figs. 51, 57). Furthermore, PEI-arg@MON@BA treatment changed macrophage distribution by decreasing pro-inflammatory M1 counts and elevating anti-inflammatory M2, and showed enhanced IL-10 level in rat serum (Fig. 7j, Supplementary Figs. 51, 57).

NMSs ameliorate inflammatory response induced by TLR9–MyD88–NF-kB signaling

To reveal the underlying therapeutic mechanisms at the gene level, we carried out transcriptomic sequencing analysis on the liver tissues of IRI rats with or without PEI-arg@MON@BA treatment. As can be seen in Fig. 8a–c, PEI-arg@MON@BA demonstrated a substantial therapeutic effect, which remarkably changed 606 genes, with 419 downregulated and 187 upregulated once compared to the control group encountering IRI. Differential GO enrichment analysis on the biological process and molecular function highlighted the differential genes after PEI-arg@MON@BA administration in vivo in response to decreased oxygen levels, response to hypoxia, ROS metabolic process, etc., which were closely associated with the pathophysiological process of IRI (Fig. 8d, Supplementary Figs. 58, 59). We also found a differential gene in the regulation of smooth muscle and a positive regulation of smooth muscle, likely due to the production of NO exhibiting vasodilation function against IRI. Moreover, after PEI-arg@MON@BA treatment, the differential gene set enrichment analysis (GSEA) enrichment analysis suggested the downregulation of HIF-1, TNF, MAPK, PI3K-Akt signaling pathways, etc., which are widely acknowledged to be associated with hypoxia, inflammatory response, as well as cell apoptosis (Supplementary Figs. 58–60). In fact, various inflammatory- and immune-related pathways, including MAPK, JAK-STAT, NOD-like

https://doi.org/10.1038/s41467-025-62968-4

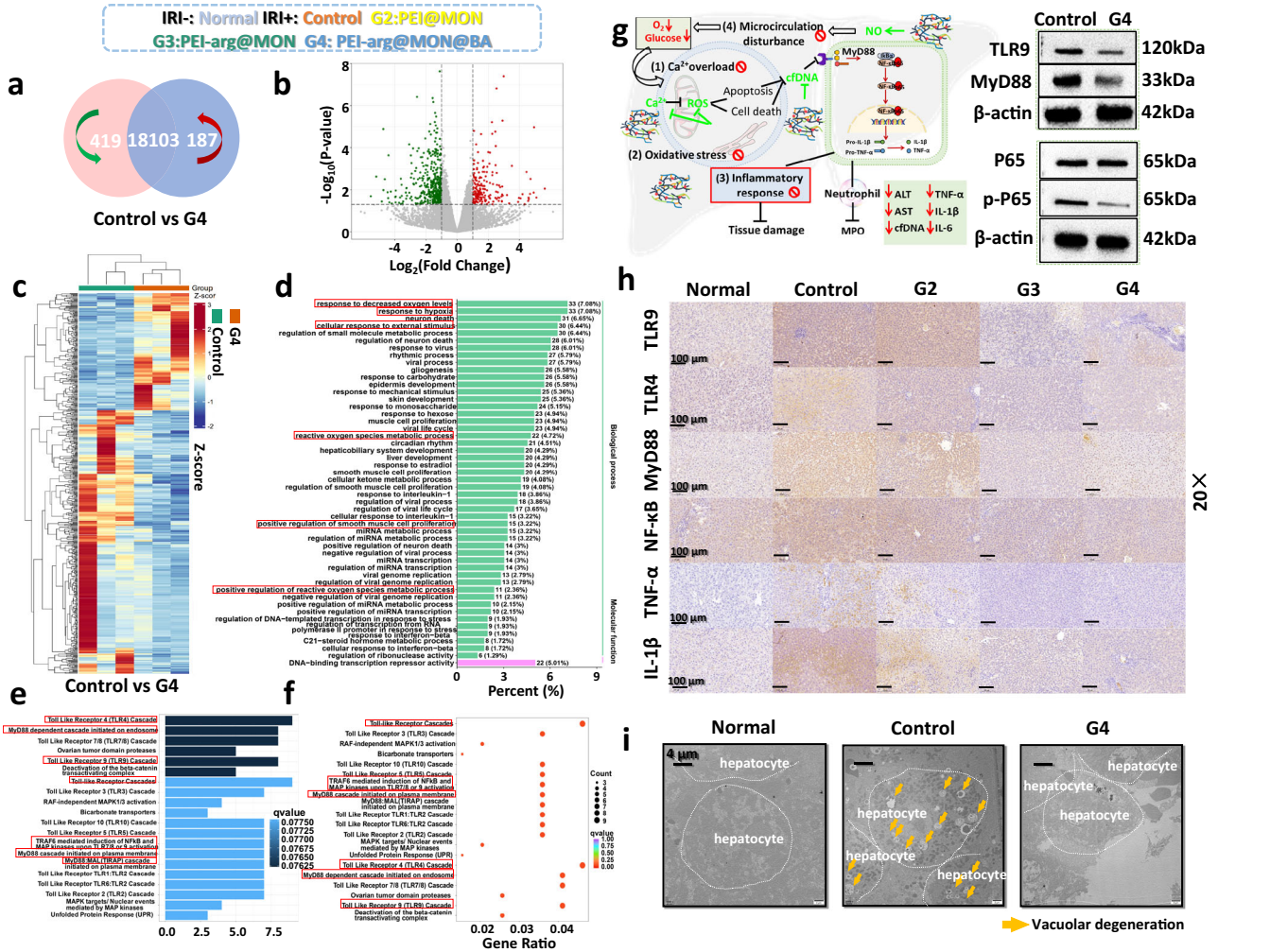

Fig. 8 | Therapeutic mechanisms of NMSs against IRI rats at 6 h post-surgery. Venn diagram (**a**), volcano plots (**b**), after performing differential analysis using the two-tailed Student's *t* test, *p* values were adjusted for multiple hypothesis testing via the Benjamini-Hochberg method), differential expressed genes (DEGs) clustering heat map (**c**), gene ontology (GO) enrichment histogram (**d**), Reactome enrichment histogram (**e**) and Reactome enrichment scatter diagram (**f**) on the IRI rats with or without PEI-arg@MON@BA treatment. **g** The therapeutic mechanism (scavenging pathogenic factors and suppress TLR9–MyD88–NF-κB signaling) and western blot (WB) analyses of TLR9, MyD88, P65, P-65 on peritoneal lavage fluid of IRI rats with or without PEI-arg@MON@BA treatment. **h** IHC images on liver tissues of IRI rats. **i** Bio-TEM images on the liver tissues of IRI rats with or without PEI-arg@MON@BA treatment. $n = 3$ biologically independent animals. Source data are provided as a Source Data file. **g** Created with BioRender.com. https://BioRender.com/tlwvys0.

receptor, FoXO, P13K-Akt showed suppression with the assistance of PEI-arg@MON@BA. These results suggested that the therapeutic mechanism of PEI-arg@MON@BA involved multiple mechanisms, including relieving hypoxia, scavenging ROS, vasodilation, alleviating inflammation, and inhibiting cell apoptosis. Reactome enrichment analysis strongly suggested a potential biological pathway of TLR9–MyD88–NF-kB, in which the expression levels of TLRs, TLR9 and MyD88-dependent cascades initiated on the endosome, etc. were adjusted for rats subjected to PEI-arg@MON@BA treatment (Supplementary Fig. 61).

To qualitatively investigate the regulation effect of NMSs on TLR9–MyD88–NF-kB signaling, the liver samples of rats were stained with antibodies against TLR9, MyD88, NF-κB, TNF-α, and IL-1β. Rats in the control group showed a larger amount of TLR9 protein, along with the elevated expression of MyD88 and NF-κB than the untreated normal rats (Fig. 8h, Supplementary Fig. 62). Rats in the PEI-arg@MON@BA groups exhibited remarkably decreased TLR9, MyD88, NF-kB, TNF-α, and IL-1β expressions. The results matched the mounting reports, which discovered that cfDNA activated TLR9 in immune cells to drive pro-inflammatory responses[19]. Furthermore, we collected the peritoneal fluids of rats and isolated macrophages to detect protein content by WB. As shown in Fig. 8g, the protein expression of TLR9, MyD88 and NF-κB (p65) was activated in macrophages in IRI rats, while the pro-inflammatory signaling pathway was significantly blocked, resulting in diminished secretion of pro-inflammatory cytokines after treatment with PEI-arg@MON@BA, and indicating that it effectively ameliorated the inflammatory response induced by TLR9–MyD88–NF-kB signaling. We also used bio-TEM to observe the liver microstructure, where healthy hepatocyte structures with less vacuolar degeneration were noticed after PEI-arg@MON@BA treatment (Fig. 8i).

Protective effect of NMSs on rat hepatic IRI model at 24 h post-IRI

At 24 h post-surgery, the decreased ALT and AST levels confirmed the partial remission of IRI, where vacuolar degeneration of hepatocytes and inflammatory cell infiltration were still found in the HE staining (SUZUKI score, 10.33, Fig. 9a, b, Supplementary Fig. 63). However, rats treated with PEI-arg@MON@BA exhibited minimal liver injury (SUZUKI score, 1.67), and the liver function indexes and pro-

https://doi.org/10.1038/s41467-025-62968-4

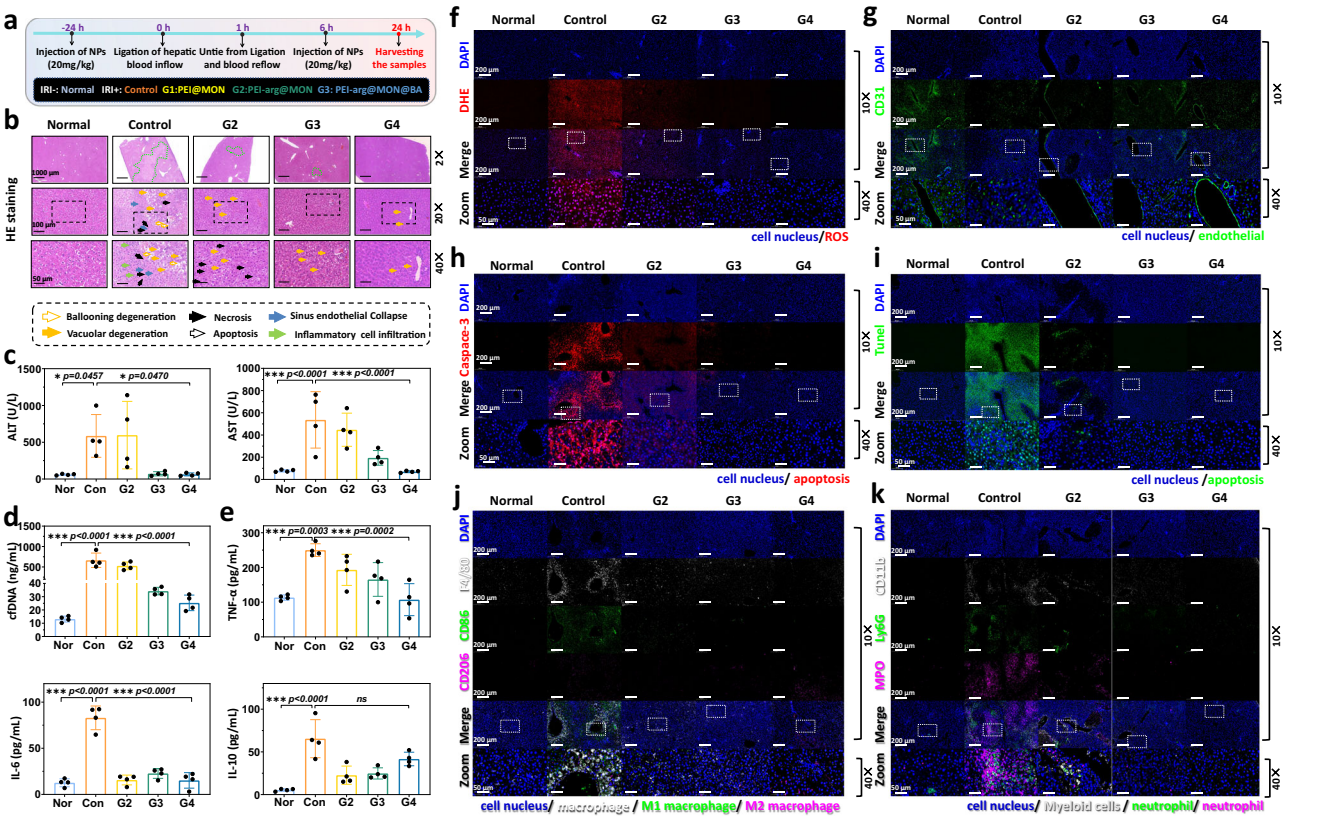

Fig. 9 | Treatment efficacy of NMSs against IRI rats at 24 h post-surgery. **a** Treatment protocols on the rat IRI model harvested at 24 h post-surgery. HE staining images (**b**), ischemic areas, SUZUKI score, and serum biochemical indexes (**c**), cfDNA level (**d**), and cytokine levels (**e**) of IRI rats after 60 min of ischemia and 24 h of reperfusion. $n = 3$ (HE staining) or 4 biologically independent animals. **f** DHE staining images of the liver tissues of IRI rats; blue: cell nucleus, red: ROS. **g** CD31 staining images of the liver tissues of IRI rats; blue: cell nucleus, green: endothelial. **h** Caspase-3 staining images of the liver tissues of IRI rats; blue: cell nucleus, red: cell apoptosis. **i** Tunel staining images of the liver tissues of IRI rats; blue: cell nucleus, green: apoptotic cells. **j** F4/80 (as a M1 macrophages marker, white), CD86 (as a M1 macrophages marker, green) and CD206 (as a M2 macrophages marker, purple) staining images of the liver tissues of IRI rats to indicate macrophages. **k** CD11b (as a myeloid cells marker, white), Ly6G (as a neutrophil marker, green) and MPO (as a neutrophil marker, purple) staining images on liver tissues of IRI rats to indicate neutrophil. $n = 3$ biologically independent animals. Data are presented as the mean ± SD. $^{*}P < 0.05$, $^{**}P < 0.01$ and $^{***}P < 0.001$ by one-way ANOVA. Source data are provided as a Source Data file.

inflammatory cytokines levels basically returned to normal (Fig. 9b–e, Supplementary Figs. 63–65). Particularly, after administration of PEI-arg@MON@BA, the rats' livers displayed almost no ROS and apoptosis signal, elucidating its protective effect against liver IRI (Fig. 9f, h, i, Supplementary Figs. 66, 67). In the IF images, rats treated with PEI-arg@MON@BA showed apparent relief on the activation of macrophages as well as on the infiltration of neutrophils, and were not much different from those of healthy normal rats (Fig. 9g, j, k, Supplementary Fig. 67). Finally, the TLR9, MyD88, NF-κB, TNF-α, and IL-1β expressions were all suppressed by NMSs (Supplementary Figs. 68, 69). In one word, the warm ischemia-reperfusion surgery offered credible evidences for the advantages of NMSs in the therapy of hepatic IRI.

Treatment prospect of NMSs on human ischemic liver

Looking forward to the therapy of PEI-arg@MON@BA against hepatic IRI in LT, we investigated its ex vivo protective effect on the human ischemic liver. We gathered the discarded diseased liver tissues from recipients in LT surgery, removed the blood, and ischemic treated the liver tissues for 2 h at 4 °C (Fig. 10a). After the ischemic procedure, HE staining demonstrated a large number of lymphocytic infiltrations and hepatocyte edema (Fig. 10d). For therapy, PEI-arg@MON@BA was dispersed in normal saline and irrigated into the liver from the portal vein to the hepatic vein for 3 h. When PEI-arg@MON@BA flowed through the portal vein, it efficiently distributed to both the tissues adjacent to blood vessels and the distal tissues due to the phagocytic function of the liver (Fig. 10b, c, Supplementary Fig. 70). Compared to the ischemic liver and normal saline–irrigated liver with plenty of lymphocytes infiltrations, the liver receiving PEI-arg@MON@BA irrigation showed only a few infiltrations of lymphocytes (Fig. 10d). As shown in Fig. 10e, f and Supplementary Fig. 71, potent ROS and apoptosis signals were generated on the ischemic-treated liver tissues. In contrast, PEI-arg@MON@BA distinctly subdued the level of ROS and apoptosis. We also studied the change of cellular phenotypes in the liver tissues after PEI-arg@MON@BA treatment via multiplex IF staining, where the proportion of activated macrophages and neutrophils in the liver was intuitively lower than that of ischemic, untreated and normal saline–treated groups, suggesting its therapeutic effect against ischemic injury (Fig. 10h, Supplementary Fig. 72–4). Furthermore, IHC images discovered certain relief on TLR9, MyD88, NF-κB and IL-1β expressions after PEI-arg@MON@BA treatment (Fig. 10g). Finally, we collected the perfusate flowing from the hepatic veins to examine the level of cfDNA and inflammatory cytokines. We found that the cfDNA and pro-inflammatory cytokines were highly overexpressed in tissues suffering from ischemic procedures, while the expressions of cfDNA, TNF-α, IL-6, IFN-γ, etc. were reduced after PEI-arg-MON@BA treatment, owing to its ability to bind cfDNA and suppress inflammation (Fig. 10i–l, Supplementary Fig. 75).

https://doi.org/10.1038/s41467-025-62968-4

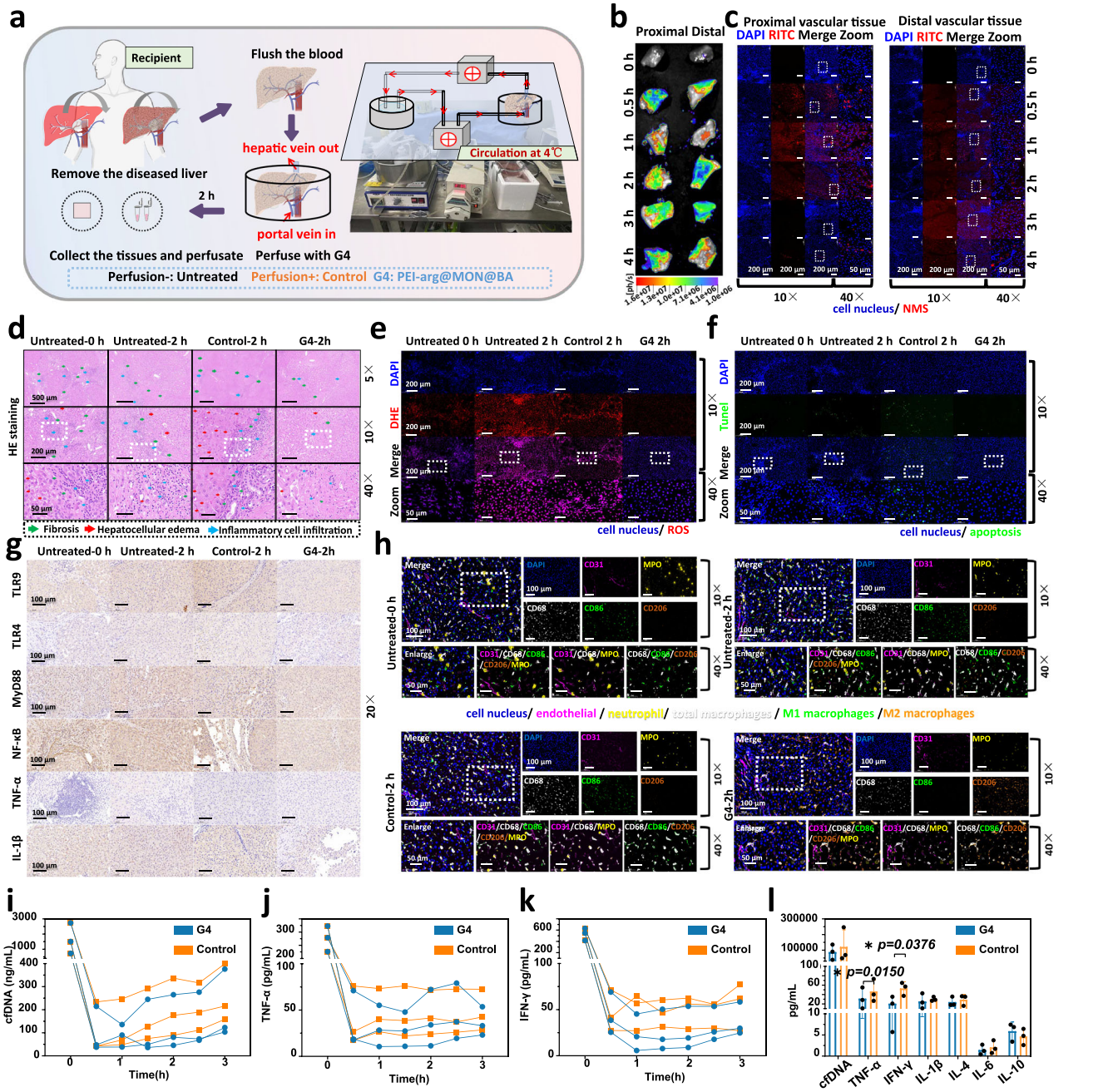

Fig. 10 | Treatment efficacy of PEI-arg@MON@BA against human ischemic liver. a. Treatment protocols on the perfusion of PEI-arg@MON@BA on human ischemic liver. Fluorescence (**b**) and CLSM (**c**) images on the distribution of PEI-arg@MON@BA from both proximal and distal vascular tissues after perfusion. HE (**d**), DHE (**e**) and Tunel (**f**) staining images on ischemic liver tissues of human; blue: cell nucleus, red: ROS, green: apoptotic cells. **g**. IHC images on liver tissues of human. **h** DAPI (as a cell nucleus marker, blue), CD31 (as an endothelial marker, pink), myeloperoxidase (MPO, as a neutrophil marker, yellow), CD68 (as a total macrophages marker, white), CD86 (as a M1 macrophages marker, green) and CD206 (as a M2 macrophages marker, orange) multiplex IF images on liver tissues of human. Dynamic perfusate cfDNA (**i**) and cytokine levels (**j**, **k**), and equilibrium concentrations (**l**) after perfusion with normal saline or PEI-arg@MON@BA. $n = 3$ biologically independent human tissues. Data are presented as the mean ± SD. $^{*}P < 0.05$, $^{**}P < 0.01$ and $^{***}P < 0.001$ by two-tailed Student's t-test. Source data are provided as a Source Data file. **g** Created with BioRender.com. https://BioRender.com/h7oi8n2.

Therefore, PEI-arg-MON@BA effectively attenuated the liver inflammation response and substantially showed a protective effect against hepatic IRI.

Protective effect of NMSs on rat LT model

Finally, we established rat orthotopic liver transplantation model by double cuff method. In a typical run, the portal vein and inferior hepatic vena cava of rats were anastomosed by cuff method, the superior and inferior hepatic vena cava were anastomosed by suture method, and the biliary tract was reconstructed by stent method. For therapy, LT rats received twice intravenous injections of PEI-arg@MON@BA (20 mg/kg) at 24 h before and 6 h after the LT surgery, respectively. At 6 and 48 h post LT, the liver lesions of rats in the control group were very severe, with spot-like necrosis and lymphocyte infiltration in the sink area (Supplementary Figs. 76, 77). After PEI-arg@MON@BA treatment, the liver lesions were mild, with only vacuolar degeneration in the cytoplasm of individual cells. No sinusoidal endothelial cell collapse, necrosis and apoptosis were observed.

The DHE staining on the liver of rats in the control group showed obvious red fluorescence, while rats in the PEI-arg@MON@BA group displayed almost no ROS signal (Supplementary Fig. 78). We also collected the blood of rats at 6, 24 and 48 h post LT surgery for biochemistry tests and inflammatory factor determination. The liver function indexes, including ALT, AST, alkaline phosphatase (ALP), albumin (ALB), total protein (TP), as well as the inflammatory cytokines, including TNF-α, IL-6, IL-1β, IL-6 and IL-17A were evident decreased following PEI-arg@MON@BA therapy, while the IL-10 and TGF-β levels were improved compared to the control groups, elucidating its protective effect against liver IRI during LT surgery (Supplementary Fig. 79).

Discussion

Hepatic IRI is closely associated with acute inflammatory responses, severe liver damage, and even multiple organ failure and death. The current treatment strategies targeting a single factor of IRI and the insufficient distribution of therapeutic agents in the liver often lead to unfavorable clinical outcomes, thus proposing an urgent need for more effective therapies. Getting back to the pathogenesis of IRI, the pathological mechanisms, including intracellular Ca^{2+} overload, oxidative stress, inflammatory response, and microcirculation disturbance, are intimately interwoven to trigger the pathophysiological cascade in IRI. For example, an increase in intracellular Ca^{2+} can activate the Ca^{2+}-dependent proteolytic enzyme, promote the transformation of xanthine dehydrogenase into xanthine oxidase, and increase the production of ROS through the xanthine oxidase system, thus damaging tissues[11]. In turn, excessive ROS injures organelles and plasma membranes, accelerating Ca^{2+} influx via transmembrane ion transport perturbations. Meanwhile, ROS and cfDNA released by the damaged cells are highly reactive mediators that can activate pro-inflammatory transcription factors, such as NF-κB, to evocate inflammatory responses[56,57]. During IRI, the overexpression of Ca^{2+} and ROS also causes an increase in endothelin secretion by endothelial cells, resulting in the concentration imbalance between endothelin and NO, directly leading to tissue microvascular contraction, microcirculation disturbance, and tissue injury. For a long time, despite the abilities of NO in regulating vascular tone, inhibiting platelet and white blood cell adhesion and improving liver microcirculation, NO is recognized as a double-edged sword in the treatment IRI, because it would quickly react with ROS to produce peroxynitrite, which causes secondary liver damage[32,58]. Thus, synchronously eliminating ROS to protect against NO oxidation is essential for NO treatment. Collectively, the complex and interactive feedback loops involved in IRI require simultaneous management of multiple pathogenic factors, inhibition on the inflammatory cascade, and target hepatic therapy to bring about substantial changes to IRI treatment.

Based on the reported pathogenesis and clinical data, we chose the pathogenic factors, including the overexpressed intracellular Ca^{2+}, cfDNA, ROS, and insufficient NO, as the primary intervention points. We designed NMSs targeting scavenging cfDNA, ROS and intracellular Ca^{2+}, and supplying NO for IRI treatment. We conducted a biomimetic silica–constructing program for the moderate and controllable formation of biosilica structures by employing PEI as a template and catalyst manipulating both the time and spatial scales of the synthesis. Employing PEI-arg@MON@BA as NMSs, the pathogenic factors cfDNA, ROS and Ca^{2+} were highly eliminated via electrostatic interaction, redox reaction, and complexing action, respectively. Meanwhile, NO was produced by the biotransformation reactions.

In light of their passive targeting ability to the liver, PEI-arg@MON@BA held a great promise for developing therapeutic strategies on hepatic diseases. Excitingly, PEI-arg@MON@BA could scavenge pathogenic factors, lessen oxidative stress, improve microcirculation, alleviate inflammation, and eventually attenuate liver damage caused by IRI. Transcriptomic analyses suggested the potential biological pathway of TLR9–MyD88–NF-κB, which was quantitatively and qualitatively verified by IHC and WB. Considering the complex pathophysiological process of the disease and the design of PEI-arg@MON@BA targeting the regulation of multiple factors in IRI, we held the opinion that more pathways corresponding to relieve oxidative stress and microcirculation homeostasis would be discovered. In addition, we also verified its protective effects against liver IRI in a rat LT model.

Besides, PEI-arg@MON@BA was proven to be stable, biocompatible, and biodegradable. Taking into account its clinical conversion potential, we investigated its therapeutic effect on the human ischemic liver. By irrigating into the ischemic liver from the portal vein to the hepatic vein, PEI-arg@MON@BA distributed to both the tissues adjacent to blood vessels and the distal tissues and efficiently reduced the level of ROS and apoptosis in the liver, highlighting its effect on relieving the ischemic injury. However, due to the technical conditions and ethical constraints, we did not investigate the function of PEI-arg@MON@BA on reperfusion injury. Indeed, the application of PEI-arg@MON@BA to patients needs to overcome many problems and challenges, including the whole-process quality control, potential side effects and long-term toxicity, in vitro and in vivo stability, pharmacokinetic/pharmacodynamic properties, and biological fate of the nanomedicine. Alternatively, PEI-arg@MON@BA could be first translated into an organic preservation solution, which would attenuate the liver inflammation response and relieve liver damage during the ischemic stage. In one word, by targeting scavenging cfDNA, ROS and intracellular Ca^{2+}, and supplying NO, the biosilica nanoparticulate scavengers with simple structure, great performance and good biocompatibility achieves targeted hepatic therapy, inhibited the inflammatory cascade, led to more attractive IRI therapy and provided valued inspiration sources for the design of nanomedicines.

Methods

Ethical statement

Our research complies with all relevant ethical regulations.

The animal studies were conducted with relevant ethical regulations under the Animal Ethics Committee of China Medical University (Protocol Number: CMU20240640). Unless otherwise stated, Sprague-Dawley (SD) rats (male, 6 ~ 8 weeks old, 200 ± 20 g) were used and housed under a specific pathogen-free environment with a 12/12 h light-dark cycle, constant temperature 24 ± 2 °C, and enough standard food and water. It needed to be noted that our research does not involve the influences of sex hormones and gender-related expression genes, and we got the clinical data and patient samples from both male and female participants, which indicated no gender-based differences. We believe that, we only used male rats in this study, as the results also went for all sexes.

The collection of patient samples was approved by the Ethics Committee of the First Hospital of China Medical University (Protocol Number: [2024]229; [2024]584; [2024]585). All participants provided written informed consent to donate their biological samples and information. Serum specimens were taken from 20 LT patients (15 male patients and 5 female patients, aged 35–73) and 20 healthy volunteers (11 male volunteers and 9 female volunteers, aged 27 to 71) at the First Hospital of China Medical University. IHC samples were collected from 12 Chinese LT patients (8 male patients and 4 female patients, aged 35 to 62). The left lateral lobes of the discarded liver were obtained from 6 recipients in LT surgery (5 male recipients and 1 female recipients, aged 51–60). Their sex and/or gender were determined according to the information provided by medical records.

RAW 264.7 cells were purchased from the Wuhan Pricella Biotechnology Co., Ltd. (CL-0190), and grown in DMEM medium (Gibco) with 10% FBS (Gibco) under a humidified atmosphere with 5% CO_2 at 37 °C. Cell lines were validated using short tandem repeat (STR) markers and were tested negative for mycoplasma contamination. AML12 cells were purchased from the Shanghai Yingwan Biotechnology Co.,

Ltd. (C2009) and grown in DMEM/F-12 medium (Gibco) with 10% FBS (Gibco) under a humidified atmosphere with 5% CO_2, at 37 °C. Cell lines were validated using short tandem repeat (STR) markers and were tested negative for mycoplasma contamination. Kupffer cells were purchased from the Shanghai Yingwan Biotechnology Co., Ltd. (C2186), and grown in RPMI-1640 medium (Gibco) with 10% FBS (Gibco) under a humidified atmosphere with 5% CO_2, at 37 °C. Cell lines were validated using short tandem repeat (STR) markers and were tested negative for mycoplasma contamination. THP-1 cells were purchased from the Wuhan Pricella Biotechnology Co., Ltd. (CL-0233), and grown in THP-1 cells specific culture medium (Wuhan Pricella Biotechnology Co., Ltd, CM-0233) under a humidified atmosphere with 5% CO_2, at 37 °C. Cell lines were validated using short tandem repeat (STR) markers and were tested negative for mycoplasma contamination.

Synthesis of NMSs

Generally speaking, this study used one-pot synthesis to prepare the NMSs without further modification. First, 0.4 mmol PEI was dispersed in 3 mL deionized water and stirred for 5 min until dissolution, followed by the addition of 0.696 g arg. After 10 min stirring constantly, the above system was transferred into the -20 °C refrigerator to induce crystalline. A few minutes later, the solid crystalline complex was added to 27 mL of deionized water pre-placed in an ice-water bath. Immediately, a mixture of 2.7 mL TEOS and 3.3 mL BTES were introduced into the mixture solution drop by drop. Next, the yellowish precipitate was collected after vigorous stirring for 24 h, separated by centrifugation at 15,000 ×g, washed with water and ethanol, and dried to obtain the PEI-arg@MON. Similarly, PEI-arg@MON@BA was prepared by the same method with the adding of 5 mg BAPTA-AM into 1 mL ethanol before the addition of mixed silica source; PEI@MON was obtained without adding arg; PEI@Si was obtained without adding arg, and BTES was changed into TEOS.

In vitro assay of cfDNA-, ROS and Ca^{2+}-scavenging capacity

To study the scavenging of cfDNA, 5 mg NMSs ($n = 3$) were dispersed in 5 mL pH 7,4 PBS containing ctDNA (1 μg/mL, GlpBio, USA), and incubated in a constant temperature oscillator at 37 °C for 4 h. At the preset time intervals, the supernatant was collected to detect the DNA concentration using the Quant-iT™ PicoGreen™ dsDNA Assay Kit (Fisher Scientific, USA). To be specific, 50 μL PicoGreen and 50 μL supernatant were added to a 96-well plate, and the fluorescence intensity was detected at 520 nm.

With the aim of quantitatively studying the elimination of Ca^{2+}, 4 mg $CaCl_2$ was dissolved in 20 mL double distilled water, and allowed to be chelated by the addition of 20 mg NMSs at 37 °C and 100 rpm. At the preset time points, the supernatant was separated by centrifugation, and the concentration of Ca^{2+} was recorded by EDTA complexometric titration using NN as an indicator. The end-point of titration was determined by sudden color changes from wine red to pure blue.

To evaluate the total oxyradical scavenging capacity of NMSs, 1 mL PEI-arg@MON ethanol solution (concentration range 0–2 mg/mL) was mixed with 1 mL DPPH ethanol solution and placed in the dark at room temperature. After incubation for 30 min at room temperature, the supernatant was measured via a multifunctional microplate reader at 520 nm. Besides, H_2O_2 can react with 100 mL ABTS (1 mg/mL) and 20 μL horseradish peroxidase (HRP, 0.1 mg/mL) to represent a blue-green color, which was used to indicate the ROS consumption of PEI-arg@MON. Specifically, 500 μL H_2O_2 (2 mM) was allowed to react with different concentrations of PEI-arg@MON dispersing in 0.5 mL water for 4 h, followed by the addition of HRP and ABTS. Afterwards, the color change of the solution was observed, and the UV absorbance of the supernatant was recorded via a multifunctional microplate reader at 415 nm.

The scavenging capacity of NMSs against hydroxyl radicals (·OH) and superoxide anions ($\cdot O_2-$) was assessed via EPR spectroscopy using a Bruker EMXPlus spectrometer. For ·OH detection, the Fenton reaction system containing 1.0 mM $FeSO_4$ and 5 mM H_2O_2 (pH = 4) was employed to generate ·OH. Freshly prepared ·OH was incubated with 100 μL PEI-arg@MON@BA (10 mg/mL) and DMPO at 37 °C for 2 min. For$\cdot O_2-$ detection, Superoxide anions were produced through a xanthine (0.5 mM)/xanthine oxidase (0.2 mM) system. The newly generated $\cdot O_2-$ was reacted with 100 μL PEI-arg@MON@BA (10 mg/mL) and DMPO under identical incubation conditions (37 °C, 2 min). Radical scavenging rates were quantified by comparing signal intensities between treated and untreated groups, with triplicate measurements performed for statistical reliability. The superoxide anion ($\cdot O_2-$) scavenging capacity of PEI-arg@MON@BA was determined using the Superoxide Anion Colorimetric Assay Kit (Elabscience, Wuhan). In this assay, 20 μL PBS suspensions (pH 7.4) of PEI-arg@MON@BA at varying concentrations ($n = 3$) were combined with 20 μL enzyme working solution and 200 μL substrate solution in microplate wells. After 20 min incubation at 37 °C, absorbance was recorded at 450 nm using a microplate reader.

For hydroxyl radical (·OH) elimination assessment, the Hydroxyl Radical Scavenging Capacity Kit (Elabscience, Wuhan) was employed. A reaction mixture containing 100 μL substrate A, 100 μL substrate B, 480 μL distilled water, 200 μL substrate C, and 20 μL PEI-arg@MON@BA ($n = 3$) was incubated at 37 °C for 20 min with absorbance measured at 510 nm. The H_2O_2 scavenging capacity was quantified using the H_2O_2 Colorimetric Assay Kit (Elabscience, Wuhan). Samples containing 500 μL H_2O_2 (0.1 mM) and 500 μL PEI-arg@MON@BA ($n = 3$) were incubated at 37 °C (100 rpm, 24 h). Post-incubation, 5 s vortexing and 10 min standing preceded absorbance measurement at 405 nm.

We then collected the LT patient serum at 6 h post-surgery, and diluted the serum into 10% serum solution by normal saline. In a typical run, NMSs was incubated in the serum solution for 4 h at a concentration of 1 mg/mL. At the preset time points, the supernatant was collected to measure the content of cfDNA and H_2O_2 via Quant-iTTM PicoGreenTM dsDNA Assay Kit and Hydrogen Peroxide (H_2O_2) Colorimetric Assay Kit (elabscience, E-BC-K102-M), respectively.

In vitro assay of NO generation

The ability of PEI-arg@MON@BA to release NO was assessed using the Griess reagent assay (Beyotime,S0021S). A calibration curve for NO concentration was first established, followed by evaluation of NO release from PEI-arg@MON@BA (0 mg/mL–20 mg/mL) in the presence of H_2O_2 (100 mM), and the UV absorbance of the supernatant was recorded via a multifunctional microplate reader at 540 nm.

Intracellular anti-oxidant and anti-inflammatory assay of NMSs

We performed the cellular evaluations on mouse RAW 264.7, THP-1 and KC cells to gain insights into the NMSs-mediated host response on macrophages. AML12 cells were employed to get information on the hepatocytes. RAW264.7, AML12, Kupffer and THP-1 cells were respectively seeded at a density of 10^4. 5000, $10^4$and 2×10^4 cells per well into 96-well plates and incubated for 12 h, following replacing the medium with 1 mL pH 7.4 PBS suspension of NMSs at various concentrations for 24 h. CCK-8 assay (Glpbio, GK10001) was performed according to the product instructions and monitored the absorbance at 450 nm. To measure the protection of NMSs from oxidative damage, cells were exposed to LPS (20 μg/mL) after adding NMSs, irritated for 4 h, and sent to CCK-8 assay.

RAW264.7 cells were seeded at a density of 10^5 cells per well into 24-well plates, and AML12, Kuffer and THP-1 cells were respectively seeded at a density of 3×10^5, 5×10^5 and 10^6 cells per well into 6-well plates, incubated for 12 h, and exposed to NMSs (60 μg/mL, $n = 3$) for 4 h. Then LPS (20 μg/mL) was added to the cells and incubated for 4 h to induce the production of ROS. Subsequently, the cells were washed twice with PBS, and incubated with the fluorescence probe (10 μM, DCFH-DA) at 37 °C for 30 min. Afterwards, the fluorescence images

were observed by CLSM and quantified the fluorescence intensity by Image J software.

Intracellular Ca^{2+} and NO levels were measured using Ca^{2+} indicators (Fluo-4) and NO indicators (DAF-FM Diacetate), respectively. 60 μg/mL NMSs were added into cells and cultured for 4 h, followed by the treatment of LPS (20 μg/mL) for another 4 h at 37 °C. Then, the cells were stained with Flou-4 (10 μM) or DAF probe (5 μM) for 30 min. After removing the excessive probe, fluorescence images were acquired by CLSM, and the fluorescence intensities were quantified by Image J software.

We also conducted Live/dead staining onto cells. Cells were first incubated with NMSs (60 μg/mL, $n = 3$) for 4 h and determined the cell viability using Live/Dead Viability assay kit (Beyotime, C2015M) according to the manufacturer's description. The cytotoxicity of NMSs was observed by CLSM and quantified the fluorescence intensity by Image J software. Furthermore, to study the antioxidant ability of NMSs, LPS (20 μg/mL) was added to the positive control group and experimental groups. After 4 h, the cells were subjected to Live/dead staining.

To determine the protective effect of NMSs from oxide damage, RAW 264.7 cells were grown in T25 flasks for 12 h, incubated with NMSs (60 μg/mL, $n = 3$) for 4 h, and irritated by LPS (20 μg/mL) for 4 h. Subsequently,), the culture supernatant was collected to measure the TNF-α level according to the manufacturer's description (TNF-α assay kit, elabscience, E-EL-M3063. As for SOD-like and CAT-like activities, the cells were lysed and analyzed by the SOD activity assay kit (Solarbio, BC0175) and CAT activity assay kit (Solarbio, BC0205), respectively.

Then the THP-1 cells were irritated with 100 μL patient serum acquired at 6 h post-surgery. After adding NMSs (60 μg/mL, $n = 3$), the system was cultured for 4 h, and sent to cell apoptosis and cell cycle analysis using cell apoptosis detection kit (APE×Bio, No. K2003) and cell cycle test kit (Best Bio, BB-4104), respectively.

In vivo distribution and passive targeting of NMSs

To study the in vivo blood circulation of NMSs, rats ($n = 3$ for each time point) were fasted overnight and injected intravenously with the normal saline suspension of PEI-arg@MON@BA (at a dose of 20 mg/kg). At the pre-designed time intervals, blood was collected and stored at -80 °C. The silica element content in the plasma was detected by ICP-MS (iCAP RQ, Thermo Scientific Co. Ltd., USA) according to the calibration curve. Moreover, rats were executed at 24 h or 7 day, where the major organs were removed, homogenized, nitration, and sent to ICP-MS to detect the distribution of the NMS. We also established rat IRI models ($n = 3$ for each time point), intravenous injected PEI-arg@MON@BA (20 mg/kg) to rats twice at 24 h before and 6 h after the IRI operation, respectively, and collected the blood and main organs to quantitatively investigate its distribution.

Besides, rats were also administrated with RITC labeled PEI-arg@MON@BA (20 mg/kg, $n = 3$ for each time point), their blood and main organs were isolated for in vivo imaging via IVIS Lumina Series III Living Image System, and the mean fluorescence signal intensity of each tissue was evaluated by ROI analysis. Immediately after the in vivo imaging, the livers were fixed in formalin, embedded in OCT, frozen sliced, stained with DAPI, observed by CLSM and quantified the fluorescence intensity by Image J software.

Treatment of NMSs on rat hepatic IRI model

Rats were randomly divided into 5 groups ($n = 4$ for each time point), including the Normal, Control, PEI@MON, PEI-arg@MON and PEI-arg@MON@BA groups. Before the surgical operation, rats were fasted overnight, shaved the abdominal hair, and disinfected with iodophor solution. Next, a midline laparotomy was performed to expose the portal triplet, which was carefully lifted using surgical forceps, and the hepatic artery and portal vein were blocked by sutures. The abdomen was sewed up with sutures immediately. Following 60 min of blocking, the sutures were removed for reperfusion, and the abdomen was sewed after verifying the absence of abnormal signs. For treatment of IRI rats, the normal saline suspensions of NMSs (20 mg/kg) were intravenously injected into rats twice at 24 h before and 6 h after the surgery. Rats in the Normal group remained untreated, while rats in the Control groups received normal saline injections. After 6 h post-surgery, part of the animals received single dose of NMSs were sacrificed to collect their blood and liver samples for biochemical analysis, cytokine determination and histopathological examination, respectively. The rest animals were administered with the second dose of NMSs, and were harvested at 24 h post-surgery.

To be specific, the serum was separated by centrifugation and sent to biochemical analysis (COBAS, INTEGRA 800, RoChe, Germany), cfDNA measurement and cytokine determination, respectively. The tissues from ischemic liver lobes were fixed in formalin, embedded in paraffin, sectioned, dewaxed, and stained with HE for histological studies. The tissues were also subjected to IF staining using antibodies against CD31, CD68, CD86, CD206, MPO, Ly6g, caspase3, F480 and NF-κB to detect disease microenvironment and the expression of pathogenic factors.

Therapeutic mechanism of NMSs against Hepatic IRI

Rats were divided into 2 groups, including the control group and the PEI-arg@MON@BA group ($n = 3$), and were exposed to IRI model. The liver tissues from IRI rats were collected at 6 h post-surgery and quickly transfered to a −80 °C refrigerator. Then the total RNA in the samples was extracted using the Trizol method according to the manufacturer's instructions. The RNA was identified and quantified by a Qubit 2.0 fluorometer and the Qsep400 (Bioptic, Jiangsu, China). Following reverse transcription of RNA to cDNA and amplification of primed cDNA by PCR. RNA-seq was performed using an Illumina NovaSeq 6000 by Majorbio Bio-Pharm Biotechnology Co., Ltd. DESeq2 was used for differential gene expression analysis between two groups, and Benjamini & Hochberg correction was applied to P values. Corrected P-values and log2 fold change were used as thresholds for significant differential expression. To explore the biological function and enriched pathways, GO, Kyoto encyclopedia of genes and genomes (KEGG) enrichment analyses and GSEA were conducted using the R package "clusterProfiler".

With respect to the potential pathway, the tissues were also subjected to IHC using antibodies against TLR9, TLR4, MyD88 and NF-κB to detect disease microenvironment and the expression of pathogenic factors.

The peritoneal macrophages from IRI rats in the control group and the PEI-arg@MON@BA group were isolated by PBS lavage at 6 h post-surgery, suspended in RPMI 1640 containing 10% fetal calf serum (FCS) and incubated at 37 °C in a humidified atmosphere with 5% CO_2 for 24 h. The adherent cells were lysed with RIPA lysis buffer containing protease inhibitor, and centrifuged to separate supernatant, which were then mixed with the Nonreducing SDS buffer. Subsequently, the system were heated, centrifuged, at stored at −80 °C. Samples (10 μg) were separated on sodium dodecyl sulfate-polyacrylamide gel electrophoresis (SDS-PAGE) and transferred to polyvinylidene fluoride (PVDF) (ISEQ00010, Millipore) membranes. After blocking with BSA, the blots were incubated with TLR9, MyD88, NF-κB p65 (phospho S536), NF-κB p65 and GAPDH antibodies, by employing GAPDH as the internal control, followed by incubation with HRP-conjugated secondary antibody. Finally, the immunoreactivity was visualized Bands were analyzed by ECL detection system (GelView 6000Pro, BLT).

Treatment of NMSs on human ischemic liver

We gathered 6 discarded diseased livers from recipients in LT surgery, removed the blood, and ischemic treated the liver tissues for 2 h at

4 °C. To simulate the portal circulation and liver absorption of nanoparticles, the normal saline suspension of PEI-arg@MON@BA (1000 mL, 0.25 mg/mL, $n = 3$) was irrigated into the ischemic liver from the portal vein to the hepatic vein for 3 h using a peristaltic pump (10 mL/min, and the perfusate was allowed to cycle back to the liver). The system was kept at 4 °C, with both the untreated tissue ($n = 3$) and the tissues mechanical perfused using normal saline ($n = 3$) as references. At the preset time intervals, 2 mL of perfusate was collected for analysis of cfDNA and cytokine levels. After the treatment procedures, HE staining, IF straining against ROS and Tunel, multiplex IF staining involving CD31, CD68, CD86, CD206 and MPO, and IHC staining against NF-κB, TNF-α, IL-1β, TLR9, TLR4 and MyD88 were performed. In addition, the ex vivo human liver were also irrigated with RITC labeled PEI-arg@MON@BA (1000 mL, 0.25 mg/mL, $n = 3$), where the tissue samples were isolated from both the tissues adjacent to blood vessels and the distal tissues, and sent for in vivo imaging via IVIS Lumina Series III Living Image System and CLSM observation, respectively.

Treatment of NMSs on rat LT model

Rats were randomly divided into 2 groups ($n = 4$ for each time point), including the Control and PEI-arg@MON@BA groups. Before the surgical operation, rats were fasted overnight. For rat donor operation, the left inferior phrenic vein was ligated, the hepatoesophageal venous plexus was severed, the right renal vein was ligated, the inferior hepatic vena cava was dissociated, the portal vein was dissociated, the pyloric vein branch and the splenic vein branch were lated, the hepatic artery was lated at the hilus, and the biliary support tube was inserted and lated. Afterwards, the portal vein was injected with normal saline, and the superior and subhepatic vena cava were cut off as the outflow tract. When the liver looked yellow and the perfusion effluents were clear, the liver was removed and stored in normal saline at 4 °C. We proceeded with the donor preparation. The portal vein and subhepatic inferior vena cava were fitted with cannula, and an 8-0 non-damaging vascular suture was suspended from the left and right posterior wall of the superior and inferior vena cava. Finally, we perform surgery on rat recipient. We used a microvascular clamp to block the inferior cava and portal veins. Subsequently, sterile saline was inserted into the main portal vein at the intersection of the left and right branches of the portal vein to block the superior and inferior hepatic vena cava. The original liver was cut and removed, and the donor liver was put into the abdominal cavity. We anastomosed the superior and inferior hepatic vena cava, and inserted the portal vein cannula and inferior vena cava cannula into the recipient portal vein and subhepatic site, respectively. To end the anhepatic stage, the superior and inferior hepatic vena cava, portal vein and inferior hepatic vena cava were opened successively. Biliary duct cannula was performed after rewarming. We irrigated the liver with warm normal saline and irrigated the abdominal cavity, followed by suturing the abdominal wall. For treatment of LT rats, the normal saline suspensions of NMSs (20 mg/kg) were intravenously injected into rats twice at 24 h before and 6 h after the surgery. Rats in the Control groups received normal saline injections. At the preset time points post-surgery, we collected the blood of rats for biochemical analysis, cytokine determination. Rats were sacrificed at 6 and 48 h post LT to harvest the liver samples for histological studies.

Statistical and reproducibility

All experiments were performed in triplicate unless otherwise stated. A representative image of three replicates from each group was shown. The results were presented as mean ± standard deviation (SD). Two tailed Student's t-test was conducted to compare experimental group and control group, while one-way ANOVA was conducted to compare more than two groups unless otherwise stated. The differences were considered statistically significant for $P < 0.05$. The levels of significance were set at the probability of $^{*}P < 0.05$, $^{**}P < 0.01$, and $^{***}P < 0.001$.

Reporting summary

Further information on research design is available in the Nature Portfolio Reporting Summary linked to this article.

Data availability

The source data generated in this study are provided in the Supplementary Information/Source Data file. The source data generated in this study have been deposited in the Figshare database under DOI code 10.6084/m9.figshare.29604950 [https://doi.org/10.6084/m9.figshare.29604950]. The sequencing data used in this study are available in the NCBI Sequence Read Archive (SRA) database under BioProject accession code PRJNA1293739 [https://www.ncbi.nlm.nih.gov/bioproject/1293739].All the other data that support the findings of this study are available within the Article and its Supplementary Information files and from the corresponding author. All data are available without restrictions. Source data are provided with this paper.

References

1. Terrault, N. A., Francoz, C., Berenguer, M., Charlton, M. & Heimbach, J. Liver transplantation 2023: status report, current and future challenges. *Clin. Gastroenterol. Hepatol.* **21**, 2150–2166 (2023).
2. Asrani, S. K., Devarbhavi, H., Eaton, J. & Kamath, P. S. Burden of liver diseases in the world. *J. Hepatol.* **70**, 151–171 (2019).
3. Lucey, M. R., Furuya, K. N. & Foley, D. P. Liver transplantation. *N. Engl. J. Med.* **389**, 1888–1900 (2023).
4. Eltzschig, H. K. & Eckle, T. Ischemia and reperfusion—from mechanism to translation. *Nat. Med.* **17**, 1391–1401 (2011).
5. Zhai, Y., Petrowsky, H., Hong, J. C., Busuttil, R. W. & Kupiec-Weglinski, J. W. Ischaemia–reperfusion injury in liver transplantation—from bench to bedside. *Nat. Rev. Gastroenterol. Hepatol.* **10**, 79–89 (2013).
6. Cannistrà, M. et al. Hepatic ischemia reperfusion injury: a systematic review of literature and the role of current drugs and biomarkers. *Int. J. Surg.* **33**, S57–S70 (2016).
7. Zhai, Y., Busuttil, R. W. & Kupiec-Weglinski, J. W. Liver ischemia and reperfusion injury: new insights into mechanisms of innate—adaptive immune-mediated tissue inflammation. *Am. J. Transplant.* **11**, 1563–1569 (2011).
8. Tong, G. et al. FGF18 alleviates hepatic ischemia-reperfusion injury via the USP16-mediated KEAP1/Nrf2 signaling pathway in Male mice. *Nat. Commun.* **14**, 6107 (2023).
9. Ye, T. et al. Protective effects of Pt-N-C single-atom nanozymes against myocardial ischemia-reperfusion injury. *Nat. Commun.* **15**, 1682 (2024).
10. Chang, W. J., Chehab, M., Kink, S. & Toledo-Pereyra, L. H. Intracellular calcium signaling pathways during liver ischemia and reperfusion. *J. Investig. Surg.* **23**, 228–238 (2010).
11. Dar, W. A., Sullivan, E., Bynon, J. S., Eltzschig, H. & Ju, C. Ischaemia reperfusion injury in liver transplantation: Cellular and molecular mechanisms. *Liver Int.* **39**, 788–801 (2019).
12. Wang, Y. et al. 1,2-bis(2-aminophenoxy)ethane- *N*, *N*, *N* ′, *N* ′-tetraacetic acid acetoxymethyl ester loaded reactive oxygen species responsive hyaluronic acid–bilirubin nanoparticles for acute kidney injury therapy via alleviating calcium overload mediated endoplasmic reticulum stress. *ACS Nano* **17**, 472–491 (2023).
13. Meng, F., Fu, Y., Xie, H. & Wang, H. Nanoparticle-assisted targeting delivery technologies for preventing organ rejection. *Transplantation* **108**, 2174 (2024).
14. Bardallo, R. G. et al. Nrf2 and oxidative stress in liver ischemia/reperfusion injury. *FEBS J.* **289**, 5463–5479 (2022).
15. Vasileiou, I. et al. Toll-like receptors: A novel target for therapeutic intervention in intestinal and hepatic ischemia–reperfusion injury?. *Expert Opin. Ther. Targets* **14**, 839–853 (2010).

16. Yao, L. et al. Piceatannol alleviates liver ischaemia/reperfusion injury by inhibiting TLR4/NF-κB/NLRP3 in hepatic macrophages. *Eur. J. Pharmacol.* **960**, 176149 (2023).
17. Han, S. J., Kim, M., Novitsky, E., D'Agati, V. & Lee, H. T. Intestinal TLR9 deficiency exacerbates hepatic IR injury via altered intestinal inflammation and short-chain fatty acid synthesis. *FASEB J.* **34**, 12083–12099 (2020).
18. Latz, E. et al. TLR9 signals after translocating from the ER to CpG DNA in the lysosome. *Nat. Immunol.* **5**, 190–198 (2004).
19. Shi, C. et al. A nanoparticulate dual scavenger for targeted therapy of inflammatory bowel disease. *Sci. Adv.* **8**, eabj2372 (2022).
20. Dawulieti, J., Sun, M., Zhao, Y., Shao, D. & Chen, L. Treatment of severe sepsis with nanoparticulate cell-free DNA scavengers. *Sci. Adv.* **6**, 7148 (2020).
21. Zhu, H., Kong, B. & Sun, Z. L. Bioinspired nanogels as cell-free DNA trapping and scavenging organelles for rheumatoid arthritis treatment. *Proc. Natl Acad. Sci.* USA **120**, 2303385120 (2023).
22. Zhang, Y. P., Liu, X. R., Yang, M. W., Yang, S. L. & Hong, F. F. New progress in understanding roles of nitric oxide during hepatic ischemia-reperfusion injury. *World J. Hepatol.* **14**, 504–515 (2022).
23. Fu, P. & Li, W. Nitric oxide in liver ischemia–reperfusion injury. in *Liver Pathophysiology* 125–127 (Elsevier, 2017).
24. Wang, Z. et al. L-Arginine-loaded gold nanocages ameliorate myocardial ischemia/reperfusion injury by promoting nitric oxide production and maintaining mitochondrial function. *Adv. Sci.* **10**, 2302123 (2023).
25. Bhatraju, P., Crawford, J., Hall, M. & Lang, J. D. Inhaled nitric oxide: current clinical concepts. *Nitric Oxide Biol. Chem.* **50**, 114–128 (2015).
26. Li, W., Meng, Z., Liu, Y., Patel, R. P. & Lang, J. D. The hepatoprotective effect of sodium nitrite on cold ischemia-reperfusion injury. *J. Transplant.* **2012**, 635179 (2012).
27. Lang, J. D. et al. A randomized clinical trial testing the anti-inflammatory effects of preemptive inhaled nitric oxide in human liver transplantation. *PLoS ONE* **9**, e86053 (2014).
28. Manning, M. W., Kumar, P. A., Maheshwari, K. & Arora, H. Post-reperfusion syndrome in liver transplantation-an overview. *J. Cardiothorac. Vasc. Anesth.* **34**, 501–511 (2020).
29. Liu, Y. et al. Activation of YAP attenuates hepatic damage and fibrosis in liver ischemia-reperfusion injury. *J. Hepatol.* **71**, 719–730 (2019).
30. Pollok, J.-M. et al. Enhanced recovery for liver transplantation: recommendations from the 2022 international liver transplantation society consensus conference. *Lancet Gastroenterol. Hepatol.* **8**, 81–94 (2023).
31. Xl, M. et al. Novel targets and therapeutic strategies to protect against hepatic ischemia reperfusion injury. *Front. Med.* **8**, 757336 (2022).
32. Mu, J. et al. Protective effect of platinum nano-antioxidant and nitric oxide against hepatic ischemia-reperfusion injury. *Nat. Commun.* **13**, 2513 (2022).
33. Fukuda, K. et al. Inhalation of hydrogen gas suppresses hepatic injury caused by ischemia/reperfusion through reducing oxidative stress. *Biochem. Biophys. Res. Commun.* **361**, 670–674 (2007).
34. Wei, Y. et al. Carbon monoxide-releasing molecule-2 (CORM-2) attenuates acute hepatic ischemia reperfusion injury in rats. *BMC Gastroenterol.* **10**, 42 (2010).
35. Wang, Y. et al. Remodeling liver microenvironment by L-arginine loaded hollow polydopamine nanoparticles for liver cirrhosis treatment. *Biomaterials* **295**, 122028 (2023).
36. Guan, Y. et al. Nanotheranostics for the Management of Hepatic Ischemia-Reperfusion Injury. *Small* **17**, 2007727 (2021).
37. Ding, Y. et al. An orally deliverable ornithine-based self-assembling polymer nanomedicine ameliorates hyperammonemia in acetaminophen-induced acute liver injury. *Acta Biomater.* **168**, 515–528 (2023).
38. Wang, L. et al. Hepatic stellate cell-targeting micelle nanomedicine for early diagnosis and treatment of liver fibrosis. *Adv. Healthcare Mater.* **13**, e2303710 (2024).
39. Bakrania, A., Mo, Y., Zheng, G. & Bhat, M. RNA nanomedicine in liver diseases. *Hepatology* **81**, 1847–1877 (2023).
40. D, N. et al. Ceria nanoparticles meet hepatic ischemia-reperfusion injury: the perfect imperfection. *Adv. Mater.* **31**, 1902956 (2019).
41. Wang, C. et al. Emerging non-viral vectors for gene delivery. *J. Nanobiotechnol.* **21**, 1902956 (2023).
42. Zhang, X. et al. Robust genome editing in adult vascular endothelium by nanoparticle delivery of CRISPR-Cas9 plasmid DNA. *Cell Rep.* **38**, 110196 (2022).
43. Zoulikha, M. et al. Pulmonary delivery of siRNA against acute lung injury/acute respiratory distress syndrome. *Acta Pharm. Sin. B* **12**, 600–620 (2022).
44. Bauer, C. A., Robinson, D. B. & Simmons, B. A. Silica particle formation in confined environments via bioinspired polyamine catalysis at near-neutral pH. *Small* **3**, 58–62 (2007).
45. Zhu, P.-X., Fukazawa, N. & Jin, R.-H. Polyethyleneimine aggregates regulated by metal cations acting as biomimetic organic reactors for silica architectures. *Small* **3**, 394–398 (2007).
46. Ford, J. & Yang, S. Directed synthesis of silica nanoparticles on micropatterned hydrogel templates tethered with poly(-ethyleneimine). *Chem. Mater.* **19**, 5570–5575 (2007).
47. Naik, R. R. et al. Controlled formation of biosilica structures in vitro. *Chem. Commun.* **21**, 238–239 (2003).
48. Matsukizono, H. & Jin, R.-H. High-temperature-resistant chiral silica generated on chiral crystalline templates at neutral pH and ambient conditions. *Angew. Chem. Int. Ed.* **51**, 5862–5865 (2012).
49. Oliveira, F. et al. Balancing gene transfection and cytotoxicity of nucleic acid carriers with focus on ocular and hepatic disorders: evaluation of hydrophobic and hydrophilic polyethyleneimine derivatives. *J. Mater. Chem. B* **11**, 4556–4571 (2023).
50. Chi, X. et al. Targeted no-releasing L-arginine-induced hesperetin self-assembled nanoparticles for ulcerative colitis intervention. *Acta Biomater.* **190**, 560–578 (2024).
51. Sun, Y. et al. Tailoring modification modules of paclitaxel prodrug nanoassemblies to manipulate efficacy and tolerance. *Nano Today* **56**, 102275 (2024).
52. Sun, B. et al. Disulfide bond-driven oxidation- and reduction-responsive prodrug nanoassemblies for cancer therapy. *Nano Lett.* **18**, 3643–3650 (2018).
53. Yang, Y. et al. Prodrug nanoassemblies bridged by mono-/di-/tri-sulfide bonds: exploration is for going further. *Nano Today* **44**, 101480 (2022).
54. Razi, S. et al. Macrophage efferocytosis in health and disease. *Cell Biochem. Funct.* **41**, 152–165 (2023).
55. Zorko, M. & Langel, Ü Cell-penetrating peptides: mechanism and kinetics of cargo delivery. *Adv. drug Deliv. Rev.* **57**, 529–545 (2005).
56. Konkova, M.S., Kaliyanov, A.A., Sergeeva, V.A., Abramova, M.S. & Kostyuk, S.V. Oxidized cell-free DNA is a factor of stress signaling in radiation-induced bystander effects in different types of human cells. *Int. J. Genom.* **2019**, 9467029 (2019).
57. Hashimoto, T. et al. Tocilizumab suppresses NF-kappa B activation via toll-like receptor 9 signaling by reducing cell-free DNA in rheumatoid arthritis. *Clin. Exp. Immunol.* **213**, 209–220 (2023).
58. Wang, Z., Jin, A., Yang, Z. & Huang, W. Advanced nitric oxide generating nanomedicine for therapeutic applications. *ACS Nano* **17**, 8935–8965 (2023).

Acknowledgements

This work was supported by the National Natural Science Foundation of China (No. 82472136 [H.L.], No.82172174 [R.D.]), Liaoning Provincial Youth Science Foundation, Category B [H.L.], and High-level Talent

Recruitment and Cultivation Program - Youth Top-notch Talent Project, China Medical University [R.D.]

Author contributions

B.Z., X.C., R.D., and Z.B. contributed equally to this work. H.L. and R.D. conceived the concept and directed the project. B.Z., X.C., and Z.B. performed the main experimental work. X.C. and T.Z. collected and analyzed the patient specimens. B.Z. and R.Z. helped with all cellular experiments. B.Z., X.C., M.X., J.L., and X.J. assisted with the animal sections. H.L. and B.Z. wrote the manuscript. All authors discussed and commented on the manuscript.

Competing interests

The authors declare no competing interests.

Additional information

Supplementary information The online version contains supplementary material available at https://doi.org/10.1038/s41467-025-62968-4.

Correspondence and requests for materials should be addressed to Heran Li.

Peer review information *Nature Communications* thanks Yong Ma and the other, anonymous, reviewer(s) for their contribution to the peer review of this work. A peer review file is available.